Applied Physics Laboratory
University of Washington

1013 NE 40th Street
Box 355640
Seattle, WA 98105-6698

206-543-1300
FAX 206-543-6785
www.apl.washington.edu

August 26, 2021

To: Dr. Kyle Becker
Office of Naval Research (Code 322)
875 North Randolph Street
Arlington, VA 22203-1995

From: Dr. Jie Yang, Principal Investigator

Subj: ONR Grant#N00014-19-1-2257, “Sediment Acoustics Modeling Using In Situ SAMS Data”

Encl: (1) Final Technical Report for Subject Grant
(2) ASA 2021 presentation “Spatial variation of sediment geoacoustic properties at the Seabed Characterization Experiment”
(3) IEEE Publication “Statistical Inference of Sound Speed and Attenuation Dispersion of a Fine-Grained Marine Sediment”
(4) Dr. Darrell Jackson “Transducer Model” manuscript
(5) SF298 for Enclosure

Enclosure (1) is the Final Technical Report for the subject grant along with 2 presented works (2,3) and one to be published manuscript (4) by the Co-PI, Dr Darrell Jackson on the project. Enclosure (5) is the SF 298 form. These documents constitute the Final Technical Report and deliverable for ONR Grant# N00014-19-1-2257.

cc: Grant & Contract Administrator, APL-UW
Office of Sponsor Programs, UW
ONR Seattle
Naval Research Laboratory
Defense Technical Information Center

Sediment acoustics modeling using in situ SAMS data

Jie Yang
Address: Applied Physics Laboratory, University of Washington, 1013 NE 40th St., Seattle, WA 98105
phone: (206) 685-7617   fax: (206) 543-6785   email: jieyang@apl.washington.edu

Award Number: N00014-19-1-2257

LONG-TERM GOALS

The long-term objective is to address the impact of sediment inhomogeneity on sound propagation and reverberation from a few hundred hertz to 10 kHz. In this band, the frequency dependencies of sound speed and attenuation are important for applications, but cannot be inferred from high-frequency data, hence direct measurement is necessary.

OBJECTIVES

The main goals of this proposed effort are to

1) obtain SCE17 sediment sound speed and attenuation in the frequency band of 600 Hz–10 kHz;
2) build a SAMS simulator that can be used to extract more detailed information including layering and gradients;
3) investigate physical mechanisms that control the frequency dependence of sound speed and attenuation over a wide range of sediment types, from coarse to fine-grain sediments using data from TREX13 and SBCEX17.

APPROACH

The recent Seabed Characterization Experiment (SBCEX17), sponsored by the Office of Naval Research, was carried out on a mud patch off the coast of New England from March 5–April 10, 2017. During SBCEX17, *in situ* measurements of sediment sound speed and attenuation were carried out in the frequency band of 600 Hz–10 kHz, using the Sediment Acoustic-speed Measurement System (SAMS).

The Sediment Acoustic-speed Measurement System (SAMS) is designed to measure sediment sound speed and attenuation simultaneously within the surficial 3 m of sediment (Yang et al., 2008, 2017, and 2019). The system is about 4.8 m tall and 5 m wide between the end points of the triangular base and the extension arm (see Figure 1). There are ten sources and 1 receiver on the SAMS tower. Among the ten sources, eight are ITC1032's, one is an ITC1007, and one is a PS800. The ITC1032's and the ITC1007 cover a frequency band of 2–10 kHz while the PS800 covers 600 Hz–2.5 kHz. The acoustic receiver is a ring transducer at the tip of the center probe being driven into the sediment.

SAMS has two independent and interchangeable drill systems: one employs a suction mechanism and the other a water jet. The suction system gives minimal disturbance to the medium around the penetrating probe, while the water jet system can help penetrate consolidated shell/sand layers. During SBCEX17, both systems were used: the suction system was used for the majority of the sites with thick mud layers, while the waterjet system was used to penetrate the sandy basement. Typically, it took about 20 minutes for SAMS to be lowered to the seafloor, about 80 m below the R/V Sharp, while it was in dynamic positioning mode. The center probe was then drilled into the sediment through motor control. Once at a desired depth, the data-taking usually takes 40 minutes and upon completion, data are transferred to the surface for analysis. There are ten sources and one receiver on the SAMS tower. The ten sources include eight ITC1032s, one ITC1007, and one low-frequency source PS800. The ITC1032 and ITC1007 cover a frequency band of 2–10 kHz, while the PS800 covers 600–2500 Hz. The acoustic receiver is a ring transducer at the tip of the center probe.

During SBCEX17, SAMS was successfully deployed at a total of 18 sites, which were chosen to coincide with coring locations. A combination of direct measurements such as cores and SAMS, as well as chirp sonar data can be used to build a geoacoustic model at the study site and to facilitate the development of physics-based sediment acoustic models.

Four priority areas were chosen and they are 1) the central area; 2) the northwest (NW) section of the main acoustic track; 3) east-west (E-W) transect with transition into shallow mud layer to the west; and 4) the “sand box” area with sandy intrusion as close to 1.5 m below the water-sediment interface (see Fig. 2, top panel). These sites were chosen to study the spatial variation of sediment sound speed in both range and depth and specifically, its relation with 1) mud layer thickness; 2) depth structure or sound speed gradient in mud; and 3) transition from mud into sandy basement.

One of the main goals of SBCEX17 is to investigate the physical mechanisms that impact sound propagation in mud. A combination of direct measurements such as cores and SAMS, as well as reflection measurements using a chirp sonar are important in order to understand quantitatively the geoacoustic properties of mud and to thus achieve the goal. The extracted geoacoustic profiles from SAMS, piston cores and vibra-cores, in addition to several hundred samples taken from the cores (with vertical spacing of 10–20 cm), will be an ideal data set to compare with physics-based sediment acoustic models for the frequency dependencies of sediment sound speed and attenuation between 600 Hz–10 kHz. For mud, there lacks an established sediment acoustic model, and therefore, *in situ* measurements from SAMS are important for comparison with models that are currently under development.

In addition, properties of mud have been measured in isolated spots, but never measured along the track where propagation data are taken. One important question is: What is the impact of sediment inhomogeneity on sound propagation in mud? With the receiver in the sediment and ten sources placed at various distances from the receiver, SAMS offers ten different geometries at every penetration depth to help determine bottom structure such as layering and sound speed gradients. During SBCEX17, data were taken at incremental depths for some stations to help resolve the vertical structure of the sediment. Fig. 3 displays a clear sound speed gradient, i.e., the deeper the penetration depth, the higher the sound speed ratio. Moreover, SAMS can be directly used to infer mud and basement layering and sound speed structure using secondary arrivals (reflections) from layers deeper than 3 m. The variation of the layering, basement depths, and corresponding changes in sediment geoacoustic properties have considerable impact on propagation.

Data from SBCEX17 have been analyzed to produce sediment sound speed in the experimental area and results have been summarized in Yang and Jackson, 2019. One interesting (and complicating) factor about SBCEX17 data was that, for all deployments, SAMS sank about 30–50 cm into the soft sediment. Therefore, all sources and the receiver were buried in mud.

Under burial conditions, it was found unanimously the signal amplitude in sediment is higher than that in water. As an example, Fig. 3 shows the comparison between the two. The in-water data were taken after the in-sediment data, aiming to take data at exactly the same depth. The in-water data were taken in shallower water so there were multiple reflections from the boundaries after 10 ms. In the zoomed-in picture, Fig. 3(b), the in-sediment data clearly precedes the in-water data, indicating a faster sound speed given their close-to-the-same geometries. Interestingly, the amplitude of the in-sediment data is higher than that for the in-water data. The same phenomena were found true for both ITC1032 and PS800.

Modeling work, therefore, needs to be carried out to simulate source performance with different loadings replicating water and mud. A transducer model has been developed (attached to this report) by collaborator Dr. Darrell R. Jackson at APL-UW. The transducer model produces complex source TVRs based on measurements of source/receiver impedances and surrounding media properties for all three types of sources to simulate acoustic signals before and after burial with the ultimate goal of obtaining sediment sound speed and attenuation.

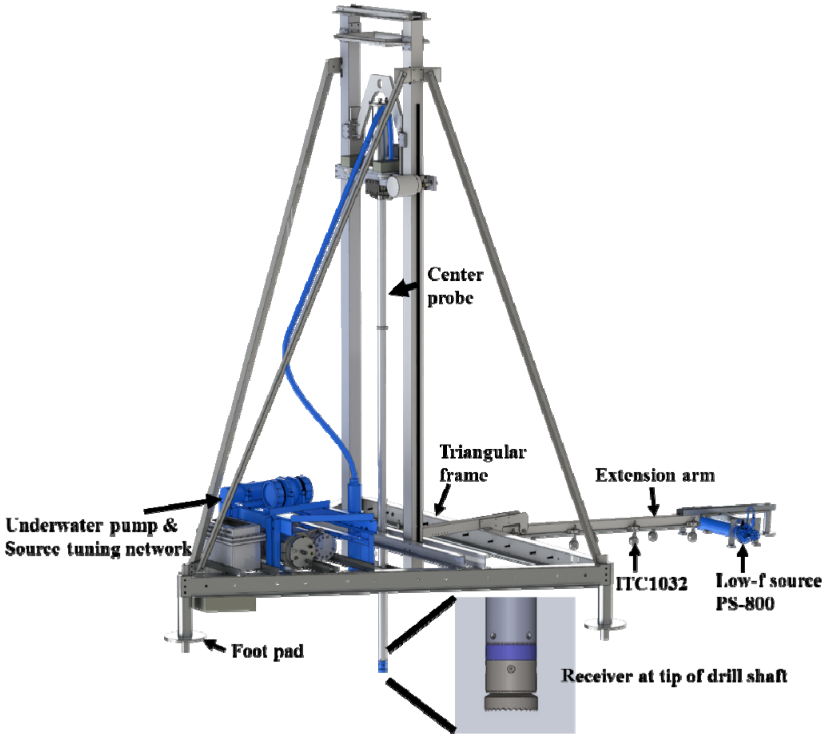

Figure 1 Sediment Acoustic-speed Measurement System (SAMS): There are eight ITC1032's, one ITC1007, and one low-frequency source PS-800 on the triangular frame and the extension arm. A ring transducer (receiver) is at the tip of the center probe that is drilled vertically into the sediment under motor control. The maximum penetration depth for the receiver is 3 m.

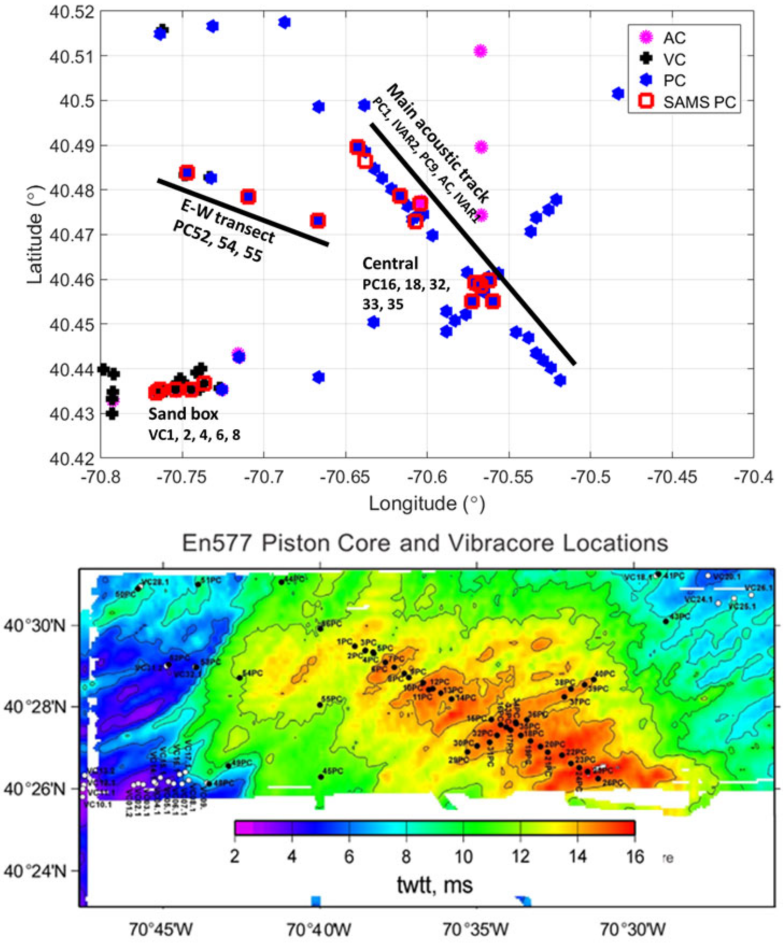

Figure 2 Top panel: SBCEX17 experimental site with four types of direct measurement locations overlaid, including acoustic (magenta), piston (blue), vibra-cores (black), and SAMS (red). The four priority areas and site names where SAMS data were taken are shown. Bottom panel: two-way travel time map of surficial mud layer with piston and vibra-core locations. (Bottom panel picture curtsey of John Goff.)

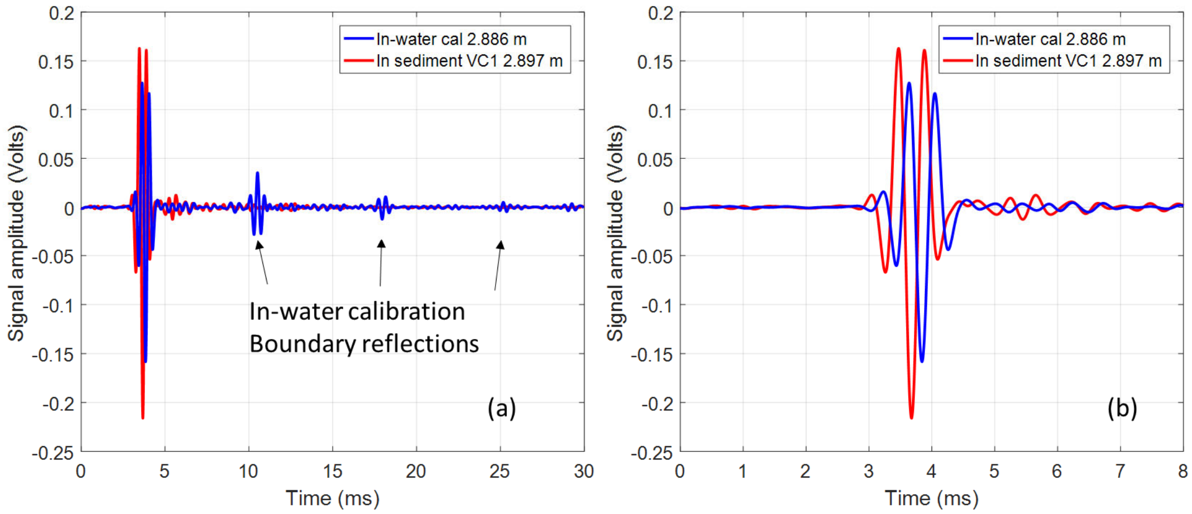

Figure 3 Acoustic data received from ITC1007. Pulse used: 1 kHz bandwidth Gaussian pulse with (b) a zoomed-in version of (a). Blue: in-water calibration data taken at a depth of 2.886 m and red: in-sediment data taken at 2.897 m, VC1 location.

WORK COMPLETED

The accomplished tasks are summarized as follows.

Task 1

During SBCEX17, SAMS was successfully deployed at 18 sites. Preliminary sediment sound speed and sediment sound speed gradient results at the 18 sites were obtained in the frequency band of 2–10 kHz. Results were summarized in a manuscript entitled “Measurement of sound speed in fine-grained sediments during the Seabed Characterization Experiment” by Jie Yang and Darrell R. Jackson 2020.

Task 2

A transducer model (manuscript attached) was developed by Dr. Darrell R. Jackson to simulate source performances before and after burial. Both signal amplitude and phase change were observed in simulated data and the changes are consistent with acoustic data.

Task 3

A lake test was completed in May 2019 with the main goal of measuring all source/receiver impedance. Data were analyzed to produce transducer model parameters to simulate signal before and after burial for ITC1032, ITC1007, and PS800.

Task 4

Completion of a SAMS simulator.

Task 5

Sediment acoustic modeling, i.e., sediment sound speed and attenuation frequency dispersion in fine-grained sediments, with *in situ* SAMS data. Manuscript published in IEEE JOE, Knobles et al., 2021.

Work in progress
With the lake test data, work is currently being done to complete the sound speed analysis in the sub-kilohertz range. Recent results were presented at ASA (presentation attached). This work demands extreme care and currently restricted to sound speed due to the fact that attenuation is tiny in fine-grained sediments.

Milestone: A paper will be submitted to the second special issue of SBCEX17, summarizing the complete SAMS results with both sound speed, attenuation, and the transducer model that has been used.

RESULTS

Results presented below show step-by-step how the transducer model and SAMS simulator developed under this project are utilized to understand in situ data. Most up-to-date progress report (Yang et al., 2021) and the Transducer Model manuscript are attached to this report.

In addition, collaboration was carried out with Knobles et al. on comparisons between inferred bottom geoacoustic parameters with in situ results from SAMS. From the inferred geophysical parameter point estimates the sediment sound speed and attenuation frequency dispersion are predicted (Knobles et al., 2021). Manuscript is attached to this report as well.

1. Sources/receiver impedance measurement and model fit results

The transducer model is attached to this report. Based on the model, there are five transducer parameters that one needs to obtain through fitting the model with measurement. The fitting procedure was repeated for ITC1032, ITC1007, and PS800. Once the five parameters are found, a complex TVR, with amplitude and phase, can be produced to simulate signals under different loading conditions, i.e., in water or mud. Model source TVR is shown here to compare with the manufacturer's nominal data.

Model fits for ITC 1032

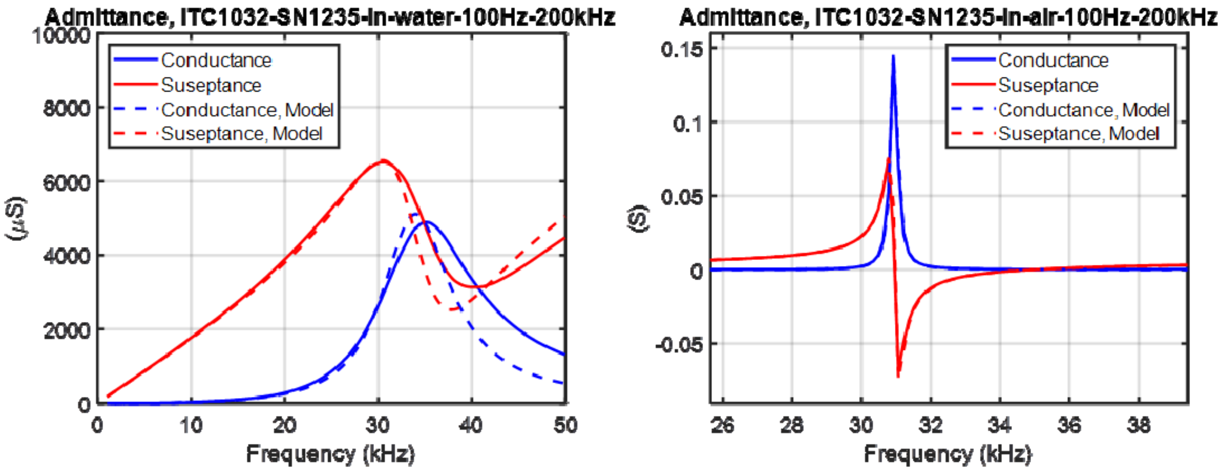

Figure 4 Left: In-water and right: in-air admittance fit between measurement and model. The admittance fit is not very good above 30 kHz, but that is far above the frequency region of interest.

The in-air fit was used to fix some of the model parameters for the ultimate hand fit. The hand fit was used to give an approximate match to the TVR data provided by the manufacturer (Fig. 3). The five model parameters are listed in the following table.

S/N 1235	f_0 (kHz)	C_0	C_T	Q	L_R	R_R
In Water	35.0	2.10e-8	6.00e-9	135	0.0041	200
In Air	30.95	2.10e-8	6.00e-9	135	0	0

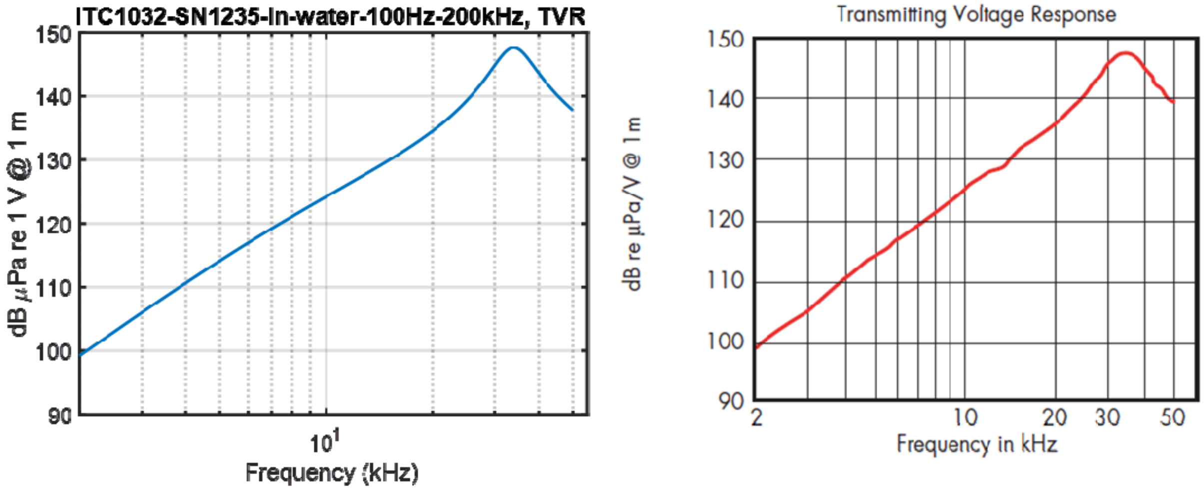

Figure 5 Left: modeled ITC1032 source TVR and right: manufacturer's standard data.

Model fits for ITC 1007

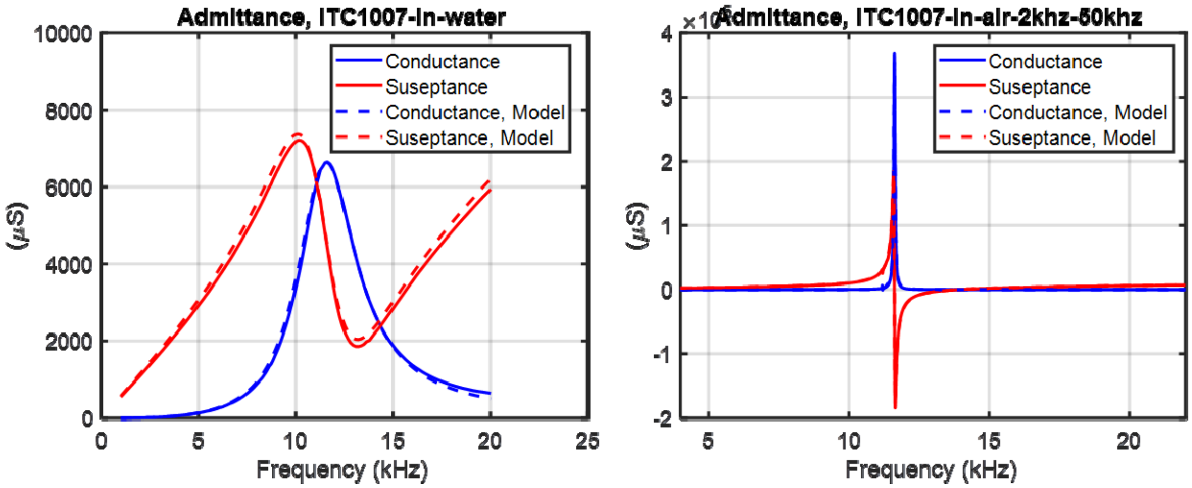

Figure 6 Left: In-water and right: in-air admittance fit between measurement and model.

	f_0 (kHz)	C_0	C_T	Q	L_R	R_R
In Water	12.10	6.30e-8	2.70e-8	180	0.0076	160
In Air	11.62	6.30e-8	2.70e-8	180	0	0

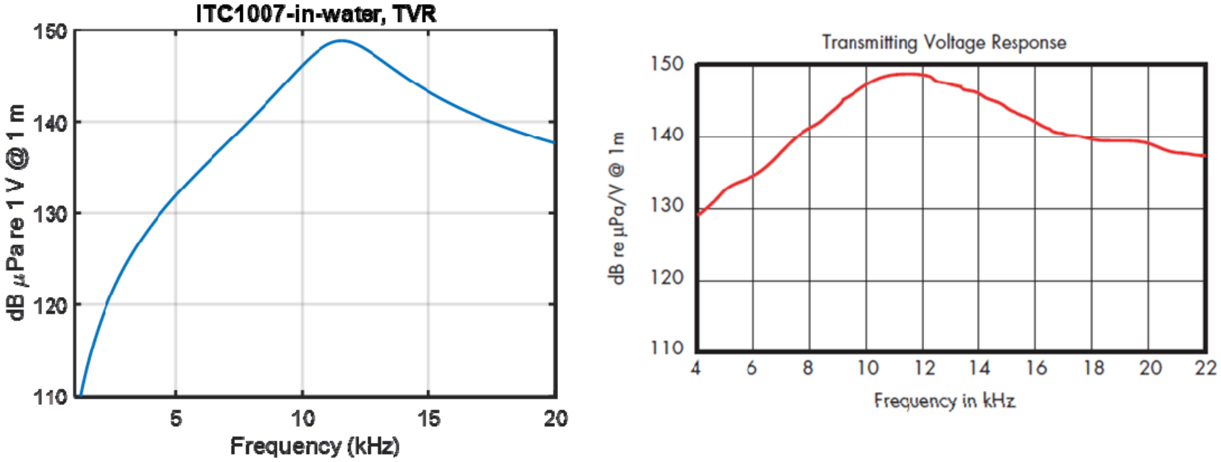

Figure 7 Left: modeled ITC1007 source TVR and right: manufacturer's standard data.

Model fits for PS800

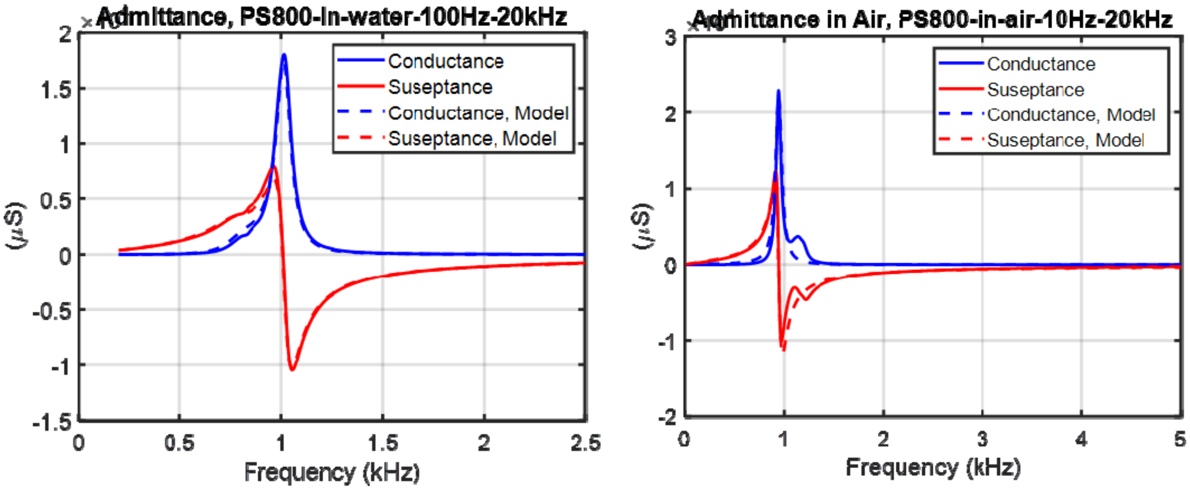

Figure 8 In-water and right: in-air admittance fit between measurement and model.

	f0 (kHz)	C0	CT	Q	LR	RR
In Water	0.875	2.71e-7	1.26e-8	4.0	0.512	3000
In Air	1.83	2.89e-7	1.07e-7	0.1	0.0177	265

The in-air fits were not used. The tuning network was used in all measurements. Separate measurements by APL gave values L_tune = 0.097 H, R_damp = 24 ohms. The latter is actually frequency dependent so the low-frequency asymptote was used, which was higher than the manufacturer's value of 18 ohms. The value for the tuning inductance agreed with the manufacturer's specifications. Hand-fitting to the in-water admittance data was crucial, as the optimization code did not fit the small feature just below 1 kHz. This feature is due to the tuning network and fitting it is essential to obtaining a reasonable TVR.

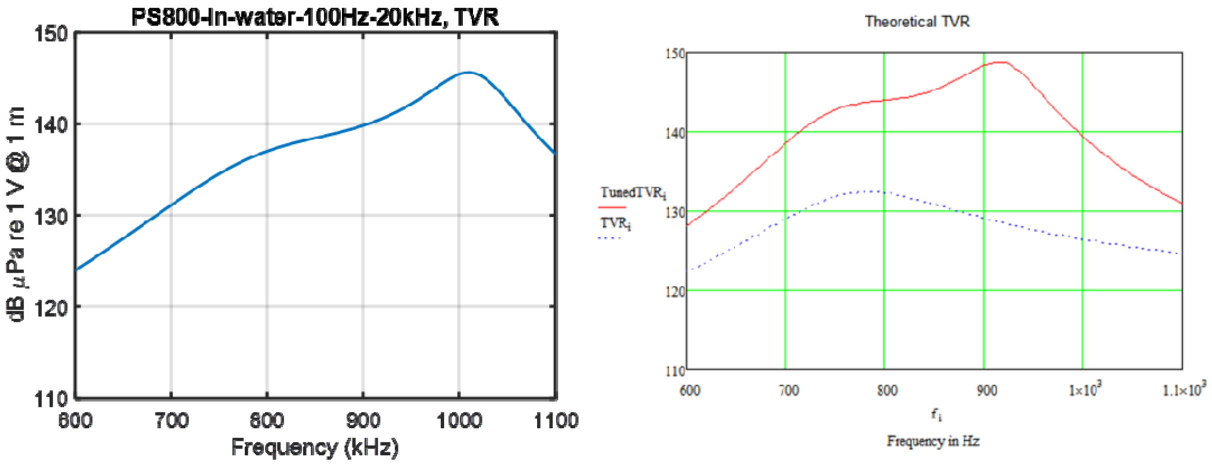

Figure 9 Left: modeled ITC1007 source TVR and right: manufacturer's standard data.

The model TVR does not fit the manufacturer's theoretical TVR very well, but it does give a reasonable fit to the in-water transmission data. It is assumed that the APL model TVR is more accurate than the manufacturer's.

2. Receiver sensitivity and directionality

Receiver sensitivity measurement was extended down to 1 kHz, as shown in Fig. 8. Receiver vertical beam pattern was also investigated (results not shown here), using a fixed source and a receiver that was placed at different depths. Little vertical beam pattern was observed in the grazing angle range of 0-45°.

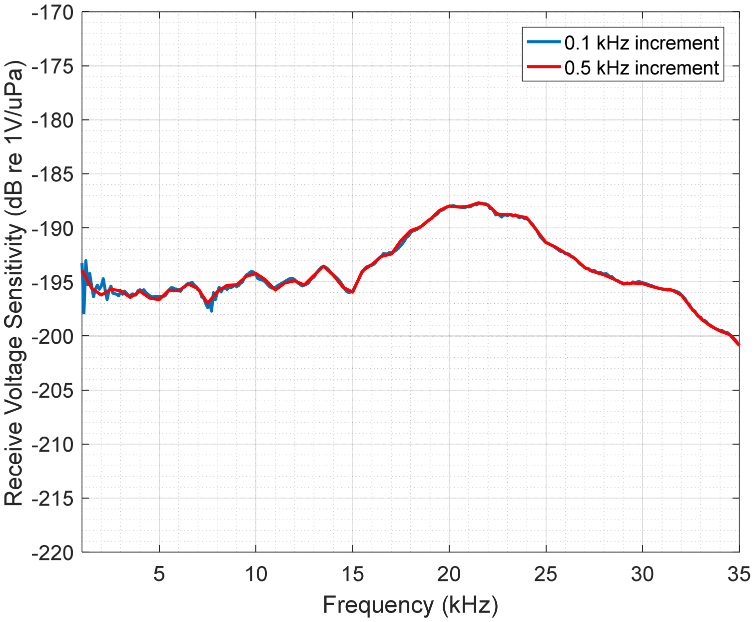

Figure 10 Measured receiver sensitivity from 1-35 kHz with 0.1 and 0.5 kHz increments.

3. Transducer modeling results

After obtaining all model parameters, the transducer model was used to predict in-water signal. The comparisons of modeled and measured in-water SAMS signals are shown for ITC1032, ITC1007, and PS800. Work is currently undergoing to match model/measured signals for the burial case, i.e., sources were buried in mud. Results are not shown here but will be included in the second paper to SBCEX17 special issue.

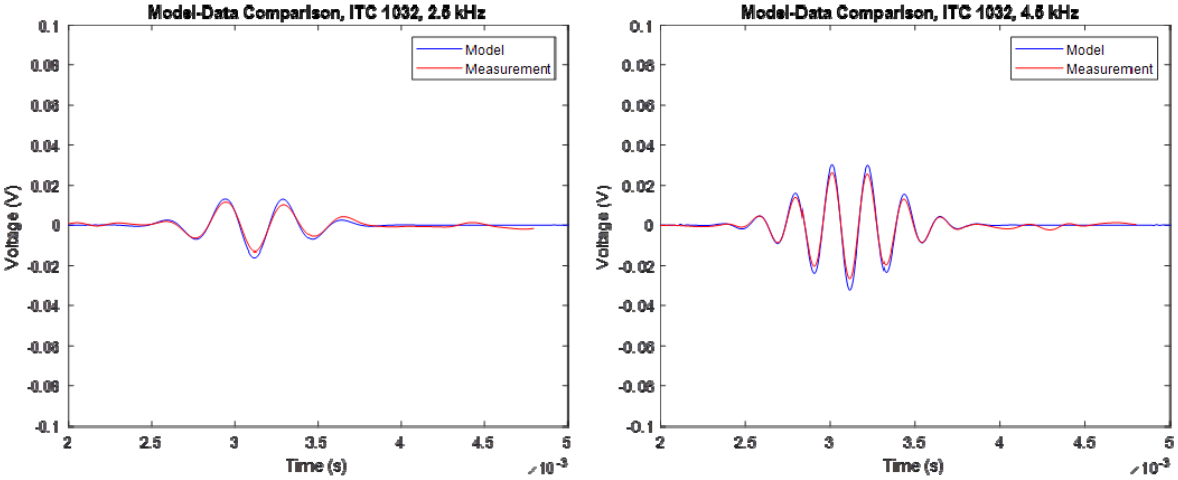

Figure 11 Comparison between ITC1032 modeled signal (blue) and in-water SAMS data (red) at center frequencies of 2.5 kHz (left) and 4.5 kHz (right).

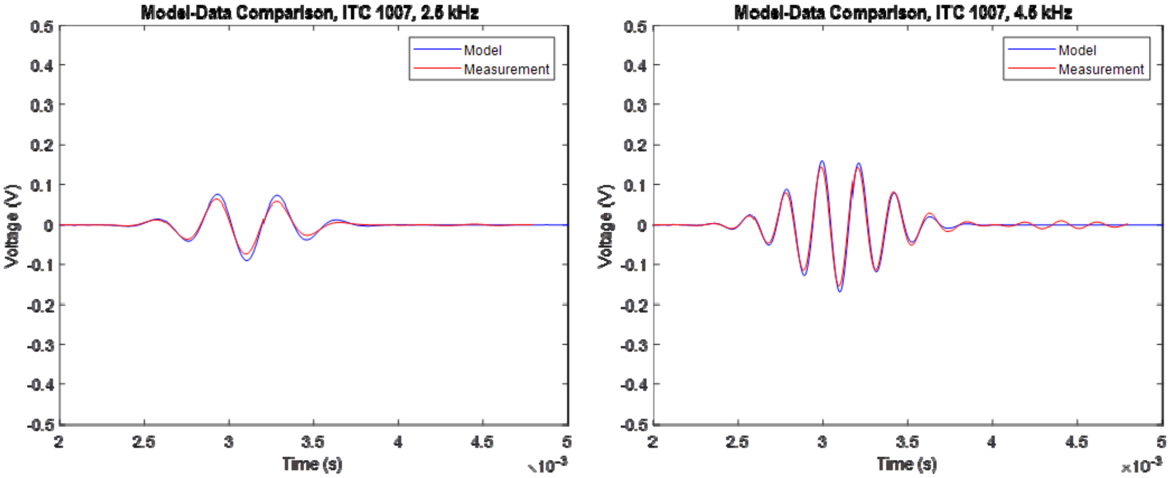

Figure 12 Comparison between ITC1007 modeled signal (blue) and in-water SAMS data (red) at center frequencies of 2.5 kHz (left) and 4.5 kHz (right).

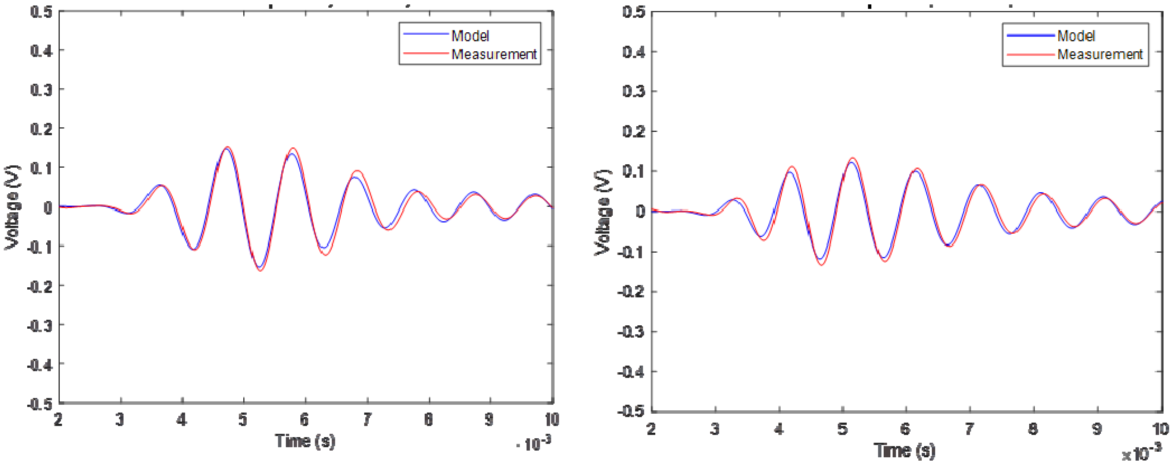

Figure 13 Comparison between PS800 modeled signal (blue) and in-water SAMS data (red) at center frequencies of 2.5 kHz (left) and 4.5 kHz (right).

IMPACT/APPLICATIONS

Naval sonar mission planning tools rely on simulation methods for propagation/reverberation modeling. One of the main limitations in making accurate predictions is the lack of a sufficiently detailed description of the environment. These environmental parameters include the properties of the sea bottom and water column over space and time. As inputs to real-time modeling, the water column properties, i.e., the sound speed profile and sea surface roughness, can be obtained in principle through direct measurements. However, sediment geoacoustic parameters, which are the most important parameters for predicting sound propagation and reverberation in many cases, are difficult to acquire directly, especially in the mid-frequency band. Work completed here and follow-on effort can be used to support detailed sound propagation prediction and validate geoacoustic inversion models, and hence, improve the accuracy in model predictions.

RELATED PROJECTS

DURIP project entitled “Enhancement of the Sediment Acoustic-speed Measurement System (SAMS)”, N00014-15-1-2808.

Project entitled “In situ measurement of sediment geoacoustic properties for ONR Seabed Characterization Experiment”, N00014-16-1-2782.

REFERENCES

D. P. Knobles, C. D. Escobar-Amado, M. J. Buckingham, W. S. Hodgkiss, P. S. Wilson, T. B. Neilsen, J. Yang, and M. Badiey, “Statistical Inference of Sound Speed and Attenuation Dispersion of a Fine-Grained Marine Sediment”, IEEE Ocean. Eng., doi: 10.1109/JOE.2021.3091846.

J. Yang and D. R. Jackson, “Spatial variation of sediment geoacoustic properties at the Seabed Characterization Experiment site”, J. Acoust. Soc. Am., 149, A150, 2021, doi.org/10.1121/10.0005369.

J. Yang and D. R. Jackson, "Measurement of Sound Speed in Fine-Grained Sediments During the Seabed Characterization Experiment," IEEE Ocean. Eng., vol. 45, no. 1, pp. 39-50, Jan. 2020, doi: 10.1109/JOE.2019.2946004.

D. R. Jackson, “A transducer model”, currently unpublished.

J. Yang, D. Tang, and K. L. Williams, “Direct measurement of sediment sound speed in Shallow Water’06,” J. Acoust. Soc. Am., 124, EL116-EL121, 2008.

Jie Yang and Dajun Tang, “Direct Measurements of Sediment Sound Speed and Attenuation in the Frequency Band of 2–8 kHz at the Target and Reverberation Experiment Site,” IEEE Ocean. Eng., Issue 99, pp. 1-8, 2017, DOI: 10.1109/JOE.2017.2714722.

D. C. Twichell and C. E. McClennen, “Morphology and processes associated with the accumulation of the fine-grained sediment deposit on the southern New England shelf," J. Sediment Petrol. 51, 269-280, 1981.

PUBLICATION

D. P. Knobles, C. D. Escobar-Amado, M. J. Buckingham, W. S. Hodgkiss, P. S. Wilson, T. B. Neilsen, J. Yang, and M. Badiey, “Statistical Inference of Sound Speed and Attenuation Dispersion of a Fine-Grained Marine Sediment”, IEEE Ocean. Eng., doi: 10.1109/JOE.2021.3091846.

J. Yang and D. R. Jackson, “Spatial variation of sediment geoacoustic properties at the Seabed Characterization Experiment site”, J. Acoust. Soc. Am., 149, A150, 2021, doi.org/10.1121/10.0005369.

Jie Yang and Darrell Jackson, “Measurement of sound speed in fine-grained sediments during the Seabed Characterization Experiment”, IEEE Ocean. Eng., vol. 45, no. 1, pp. 39-50, Jan. 2020, doi: 10.1109/JOE.2019.2946004.

Spatial variation of sediment geoacoustic properties at the Seabed Characterization Experiment

ASA Virtual Meeting

June 6–8, 2021

Jie Yang

Darrell R. Jackson

John Goff

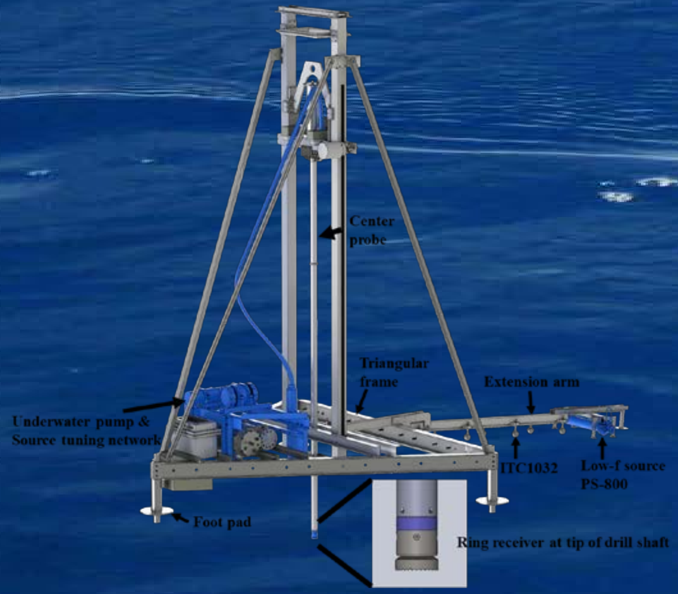

SBCEX17

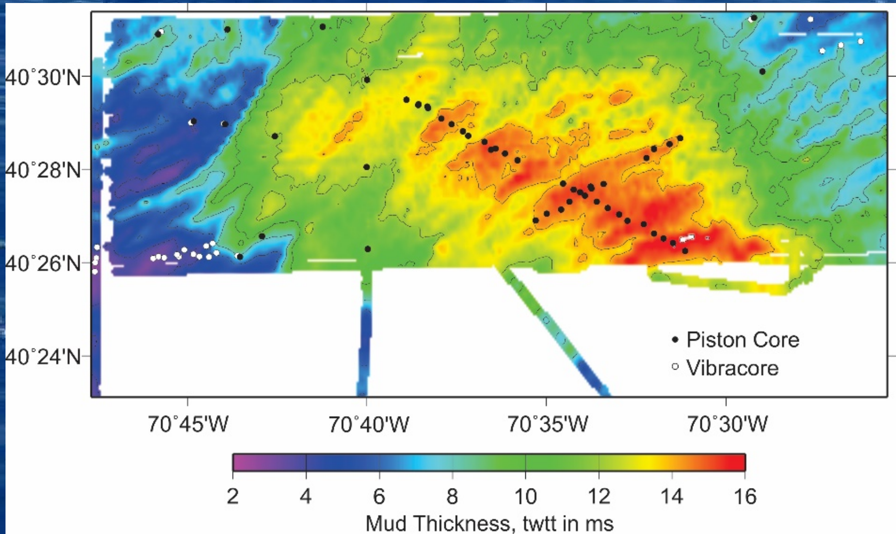

Goals and Technical Approach

Goals

- Expand sediment sound speed results in sub-kilohertz range for SBCEX17
- Study the spatial variation in both range and depth at the SBCEX17 site

Technical Approach

- Obtain sediment sound speed results in sub-kilohertz range through transducer modeling
- Compare results with those obtained in the mid-frequency range (2 – 10 kHz) and porosity measurements from J. Goff

SBCEX17

18 Sites among the four priority areas with co-located cores

Frequency band:
600 Hz – 10 kHz

Reported: 2 – 10 kHz

New: 700 – 1000 Hz
Using source PS800

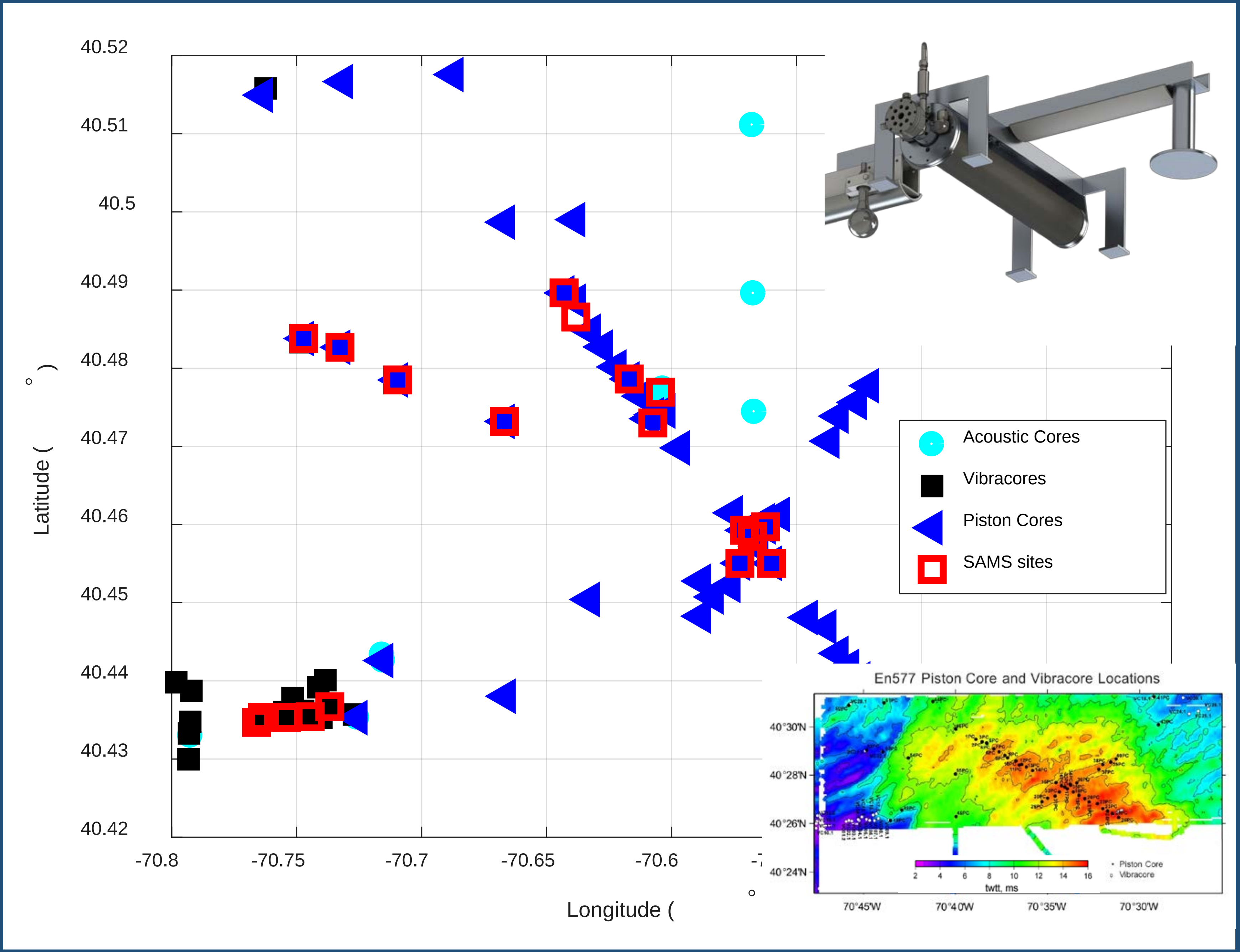

Data before/after burial

Both in-water and in-sediment data were taken with the same geometry, but in-sediment data exhibits higher amplitude

Example center frequency: 750 Hz

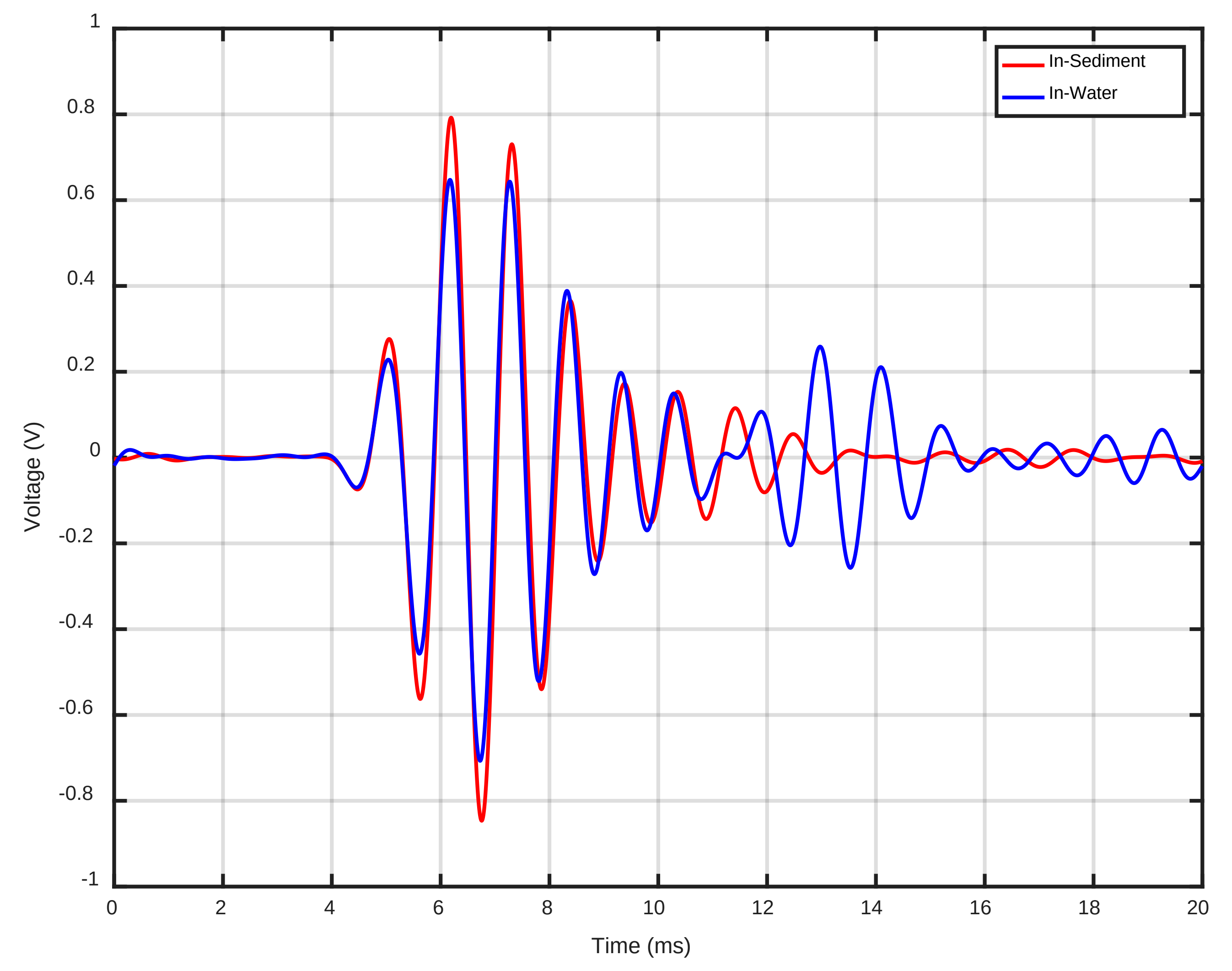

Model for SAMS Transducers

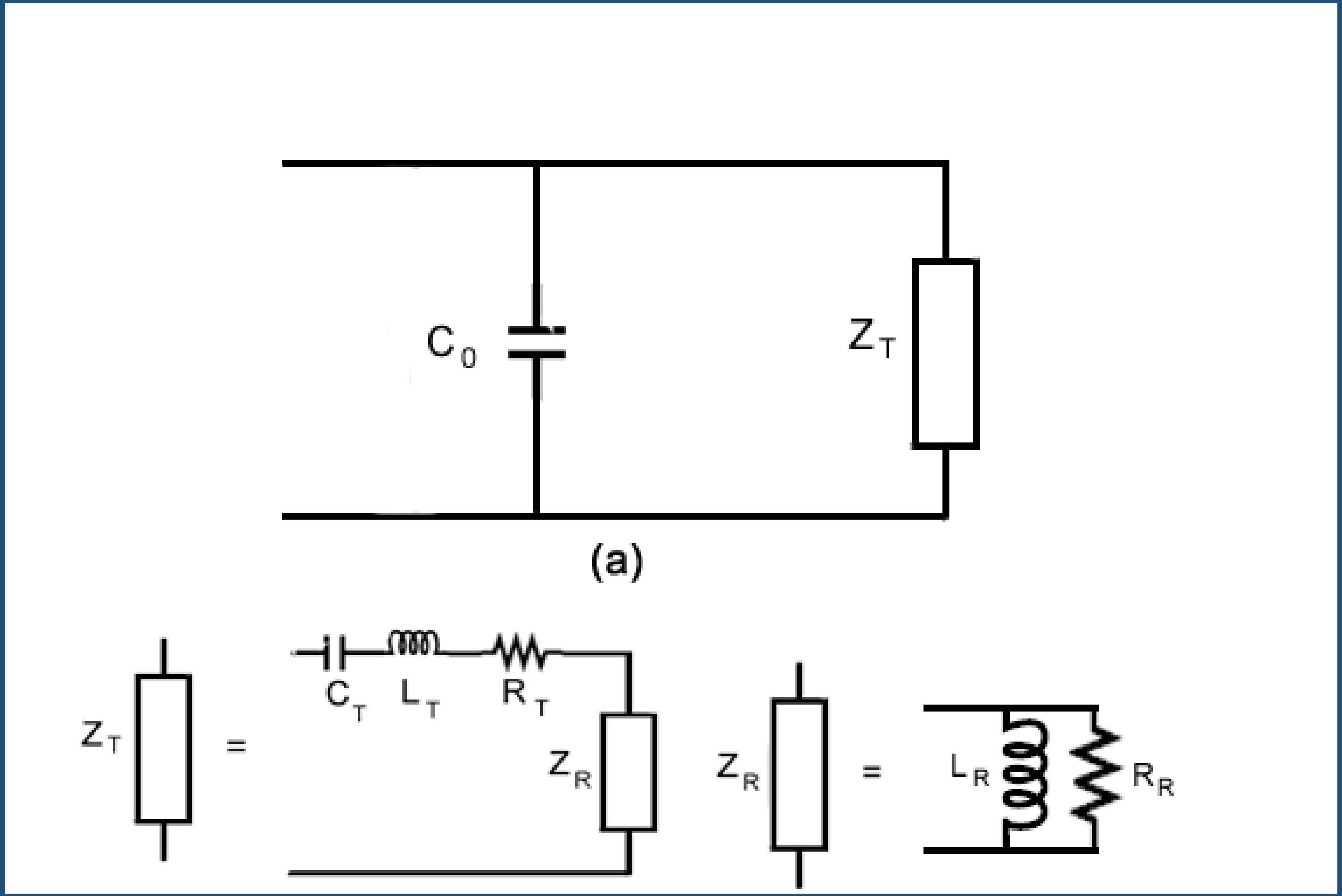

Additional resonant modes are represented by adding more Z_T in parallel.

Power dissipated in R_R is assumed to spread omnidirectionally

Measured and Modeled (2 Modes) Admittance and Transmit Voltage Response (TVR) for PS800

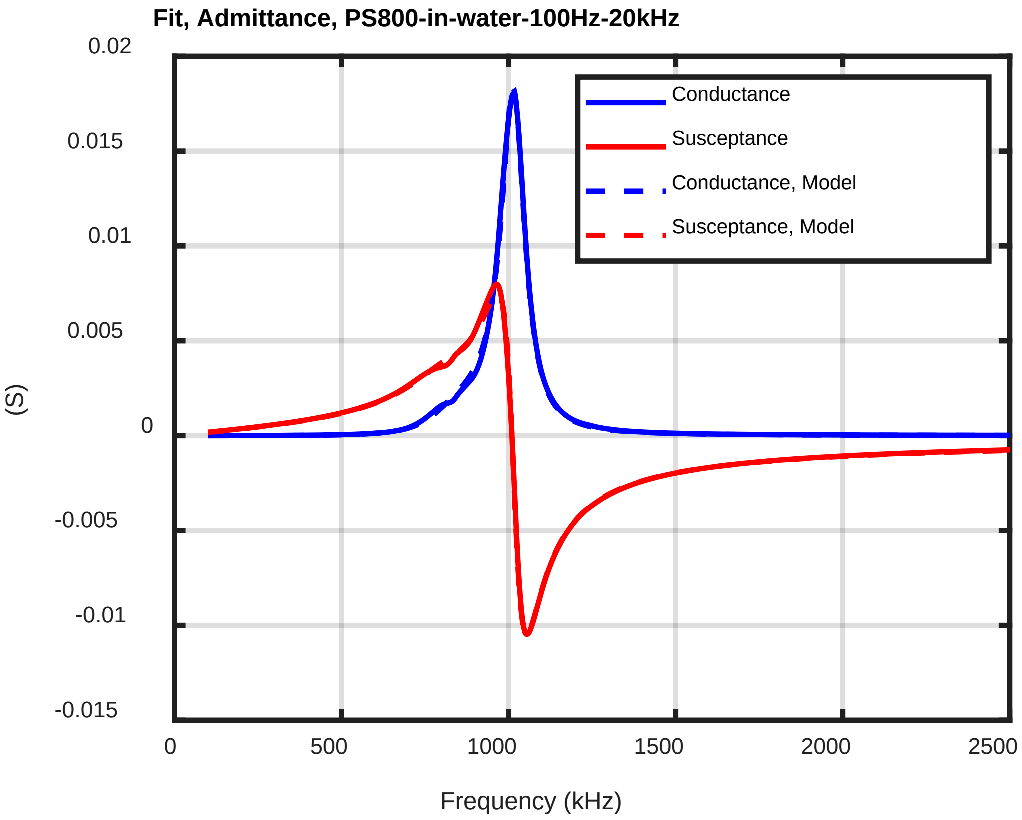
Fit, Admittance, PS800-in-water-100Hz-20kHz

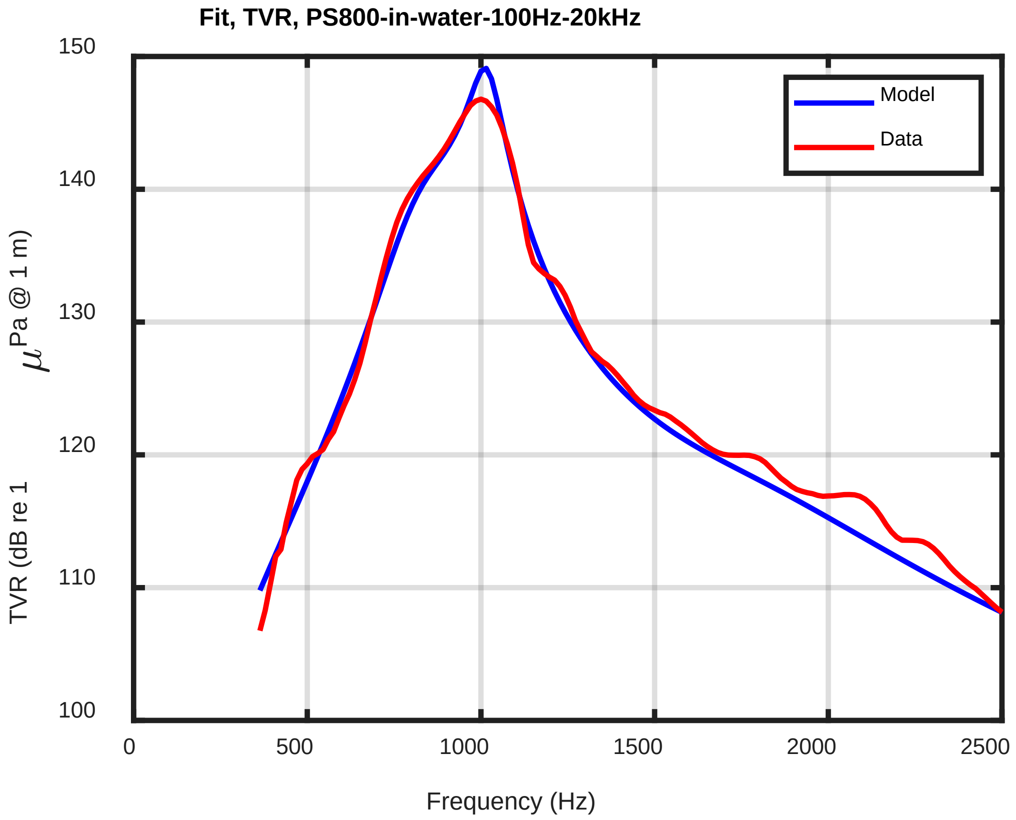
Fit, TVR, PS800-in-water-100Hz-20kHz

Model for SAMS Cable

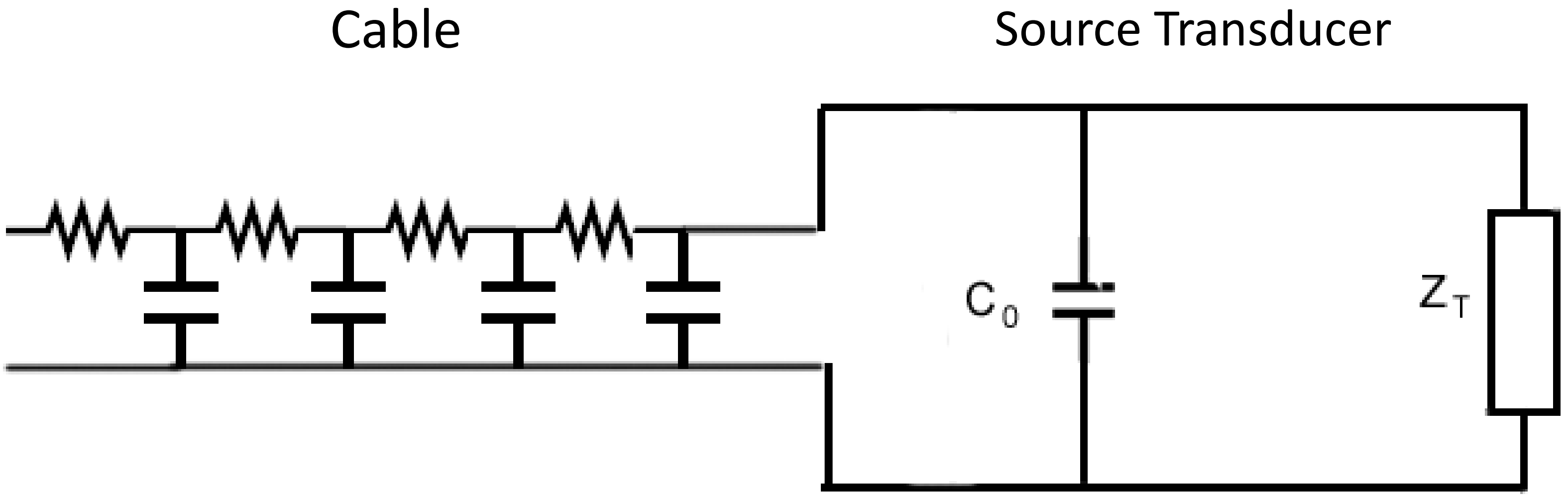

Capacitance of 0.06 μF is distributed over 250-m cable length. Round-trip resistance is 26.5 Ω.

Modeled Admittance and TVR Without and With SAMS Cable

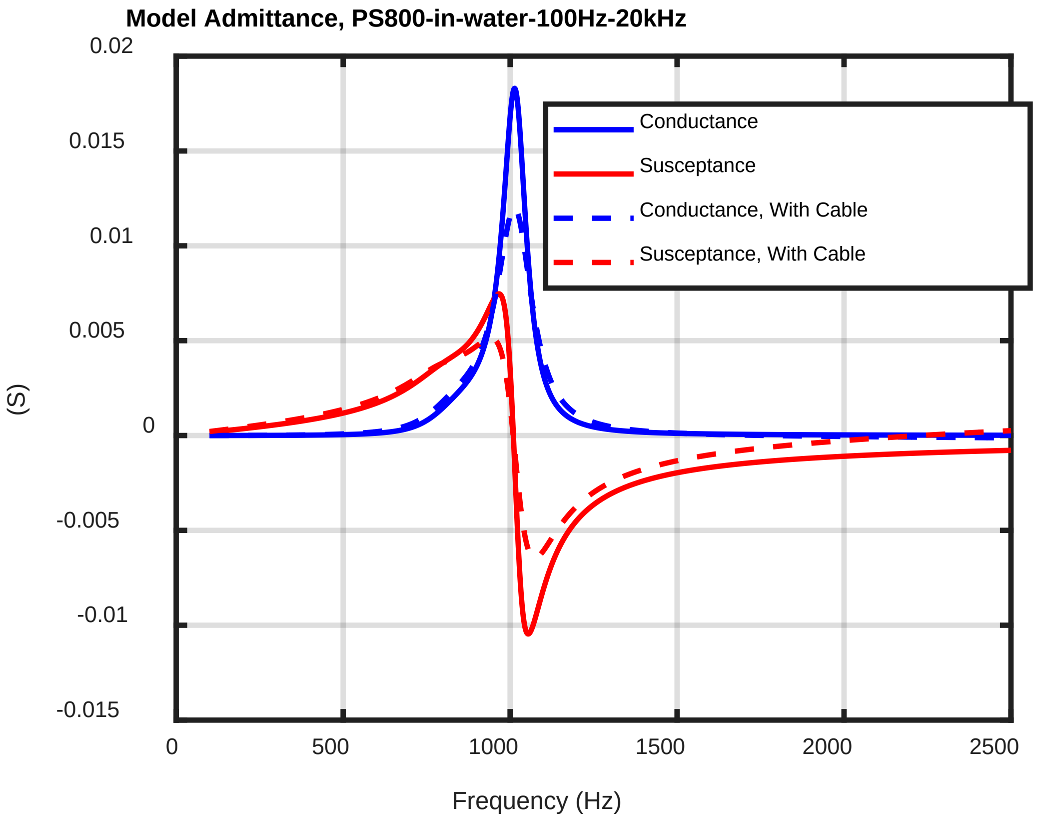

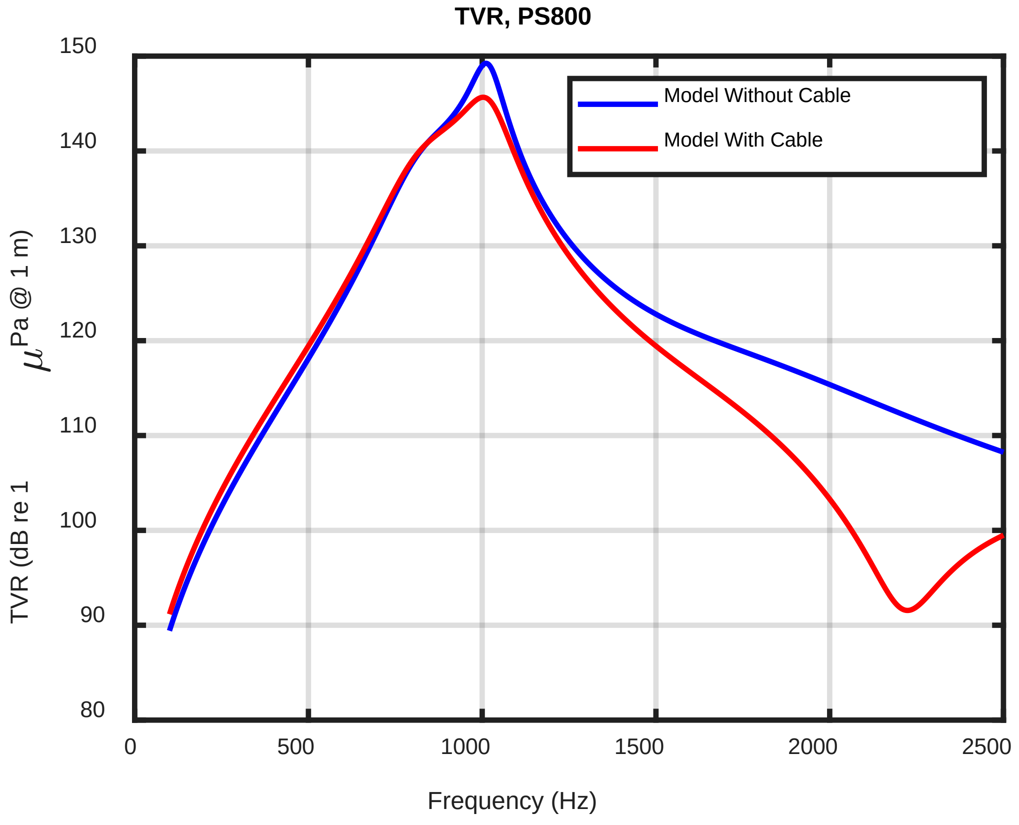

Example

In-water data/model comparison

Center frequency:

750 Hz

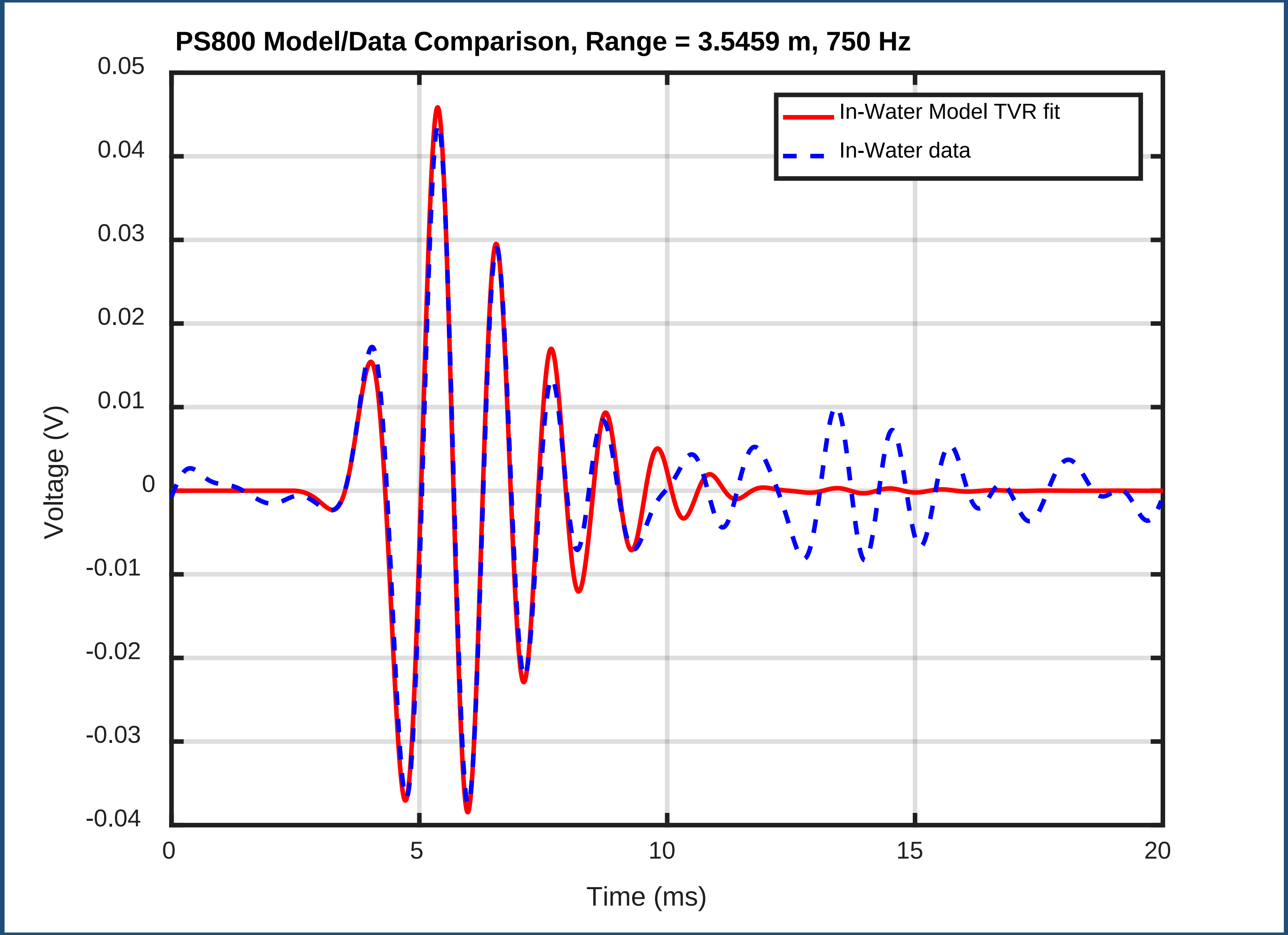

Example

In-sediment data/model comparison using normalized data

Center frequency:

750 Hz

Sound speed ratio through best fit: 0.986

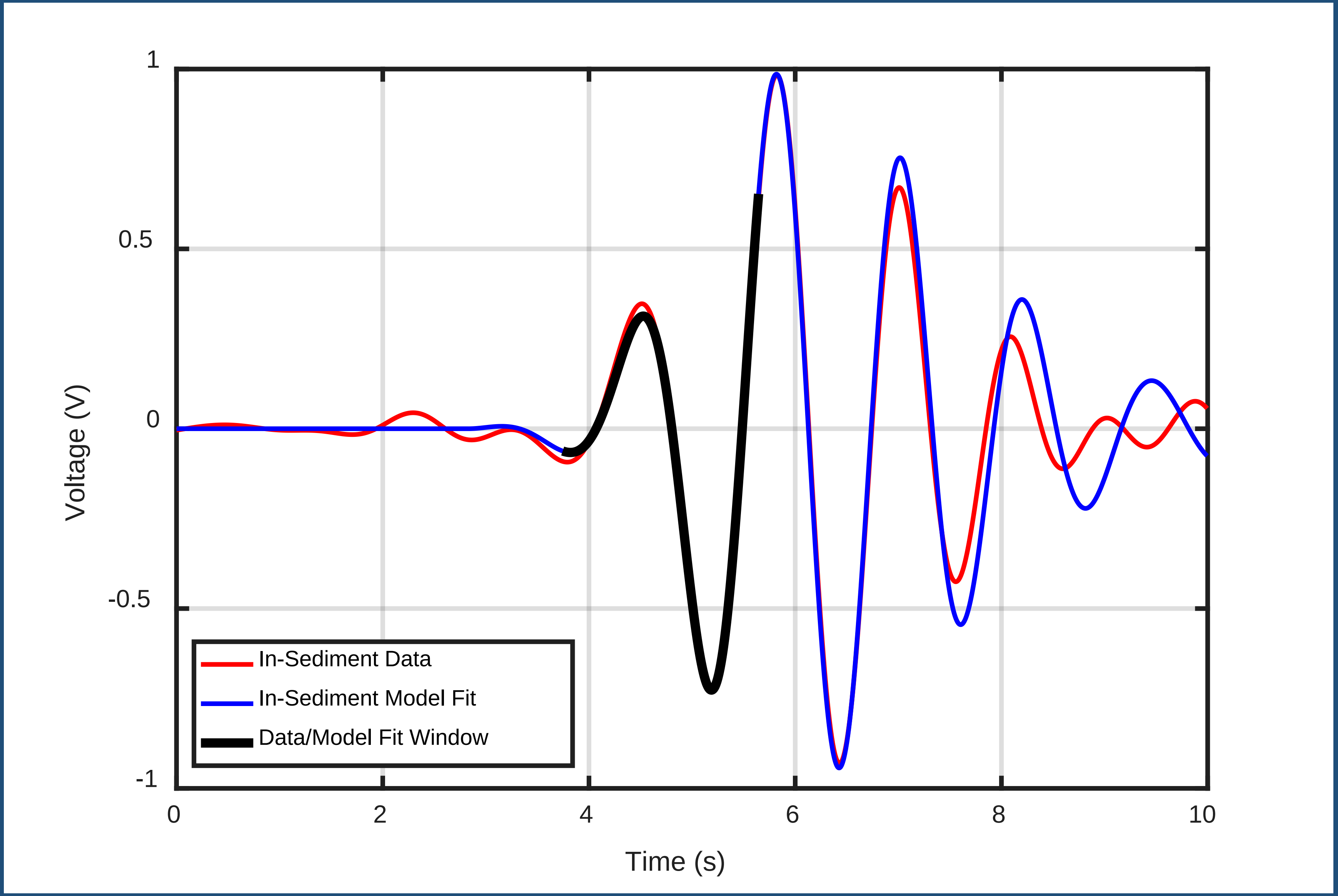

Comparison of sound speed ratio

central box, 5 sites

water sound speed: 1471 m/s

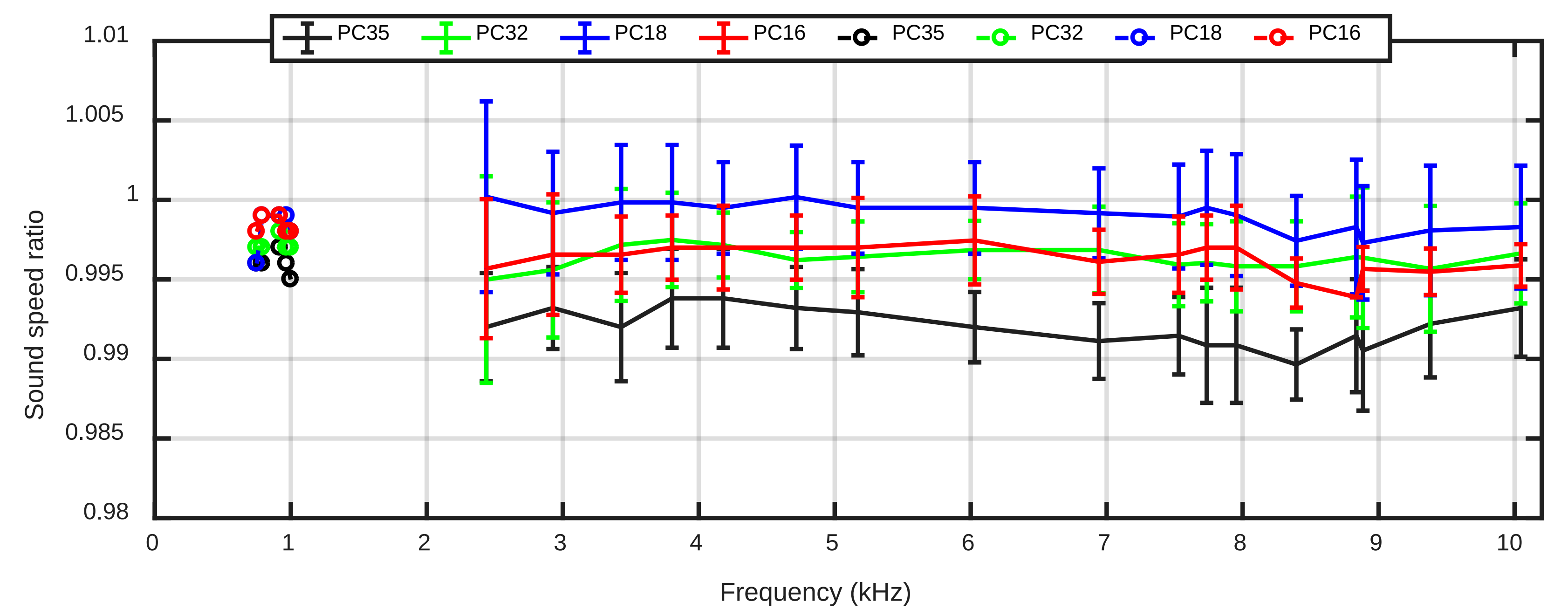

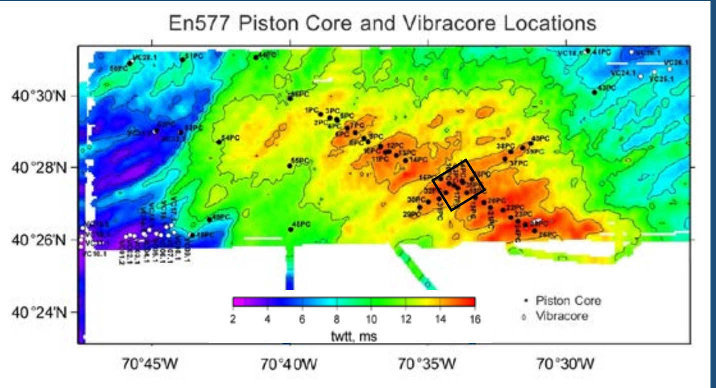

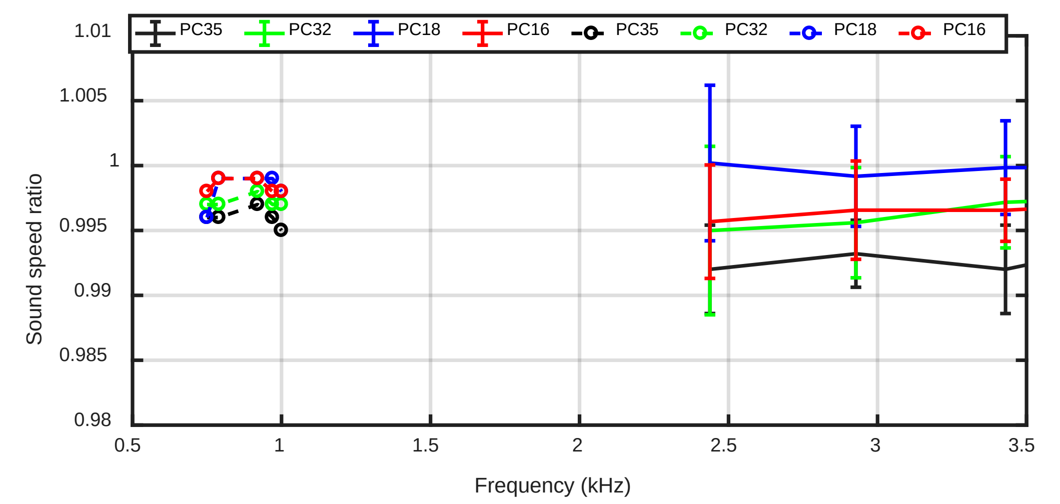

Comparison of sound speed ratio

4 sites,
NW-SE long transect

water sound speed: 1471 m/s

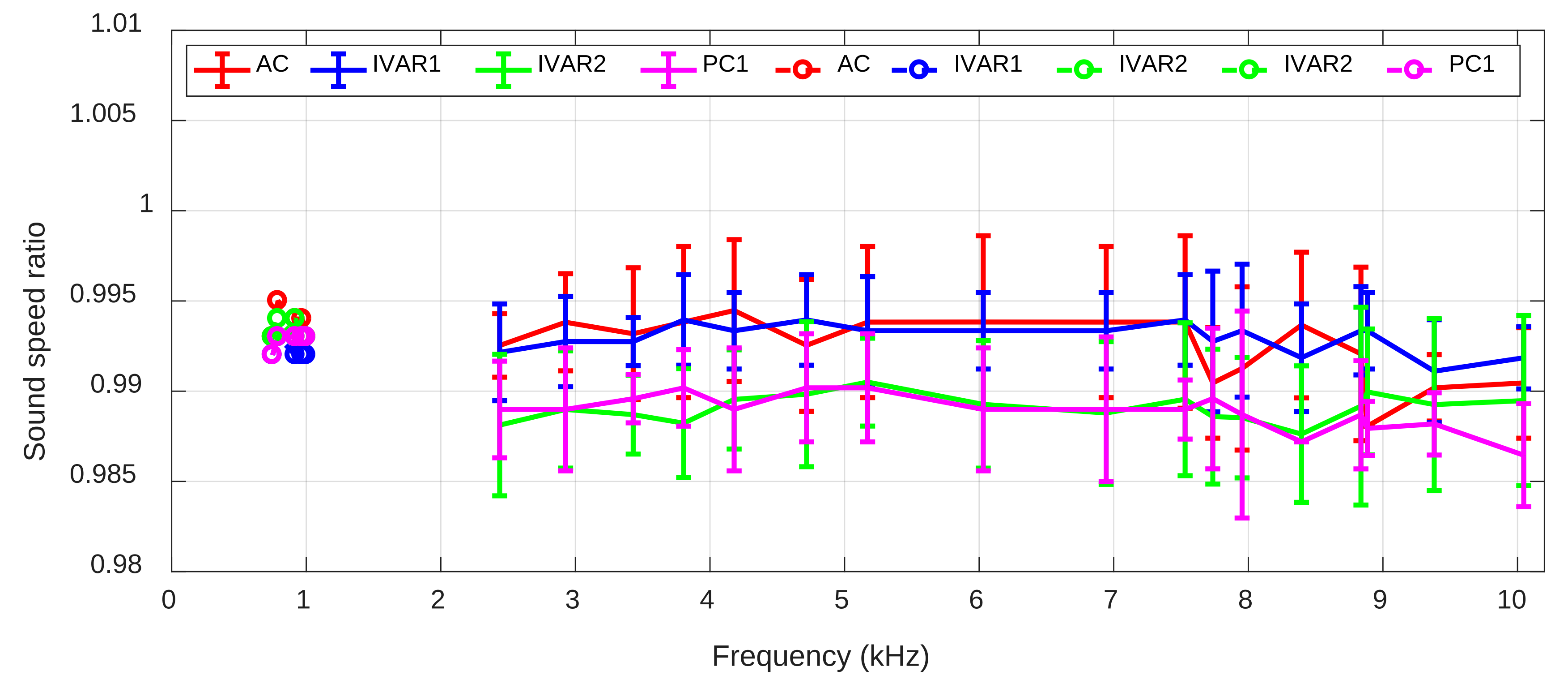

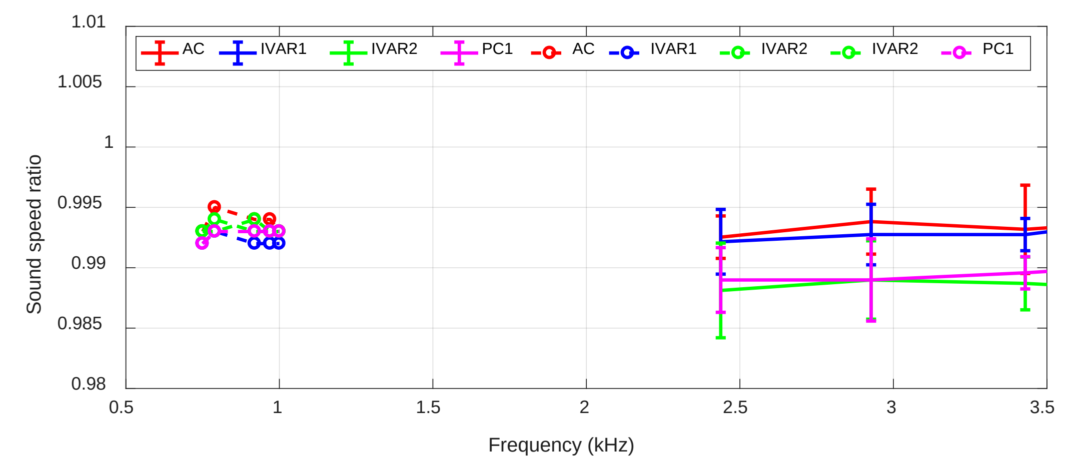

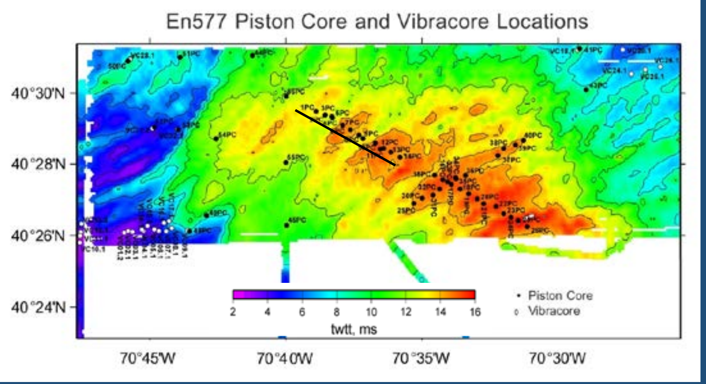

Comparison of sound speed ratio

3 sites, west transect

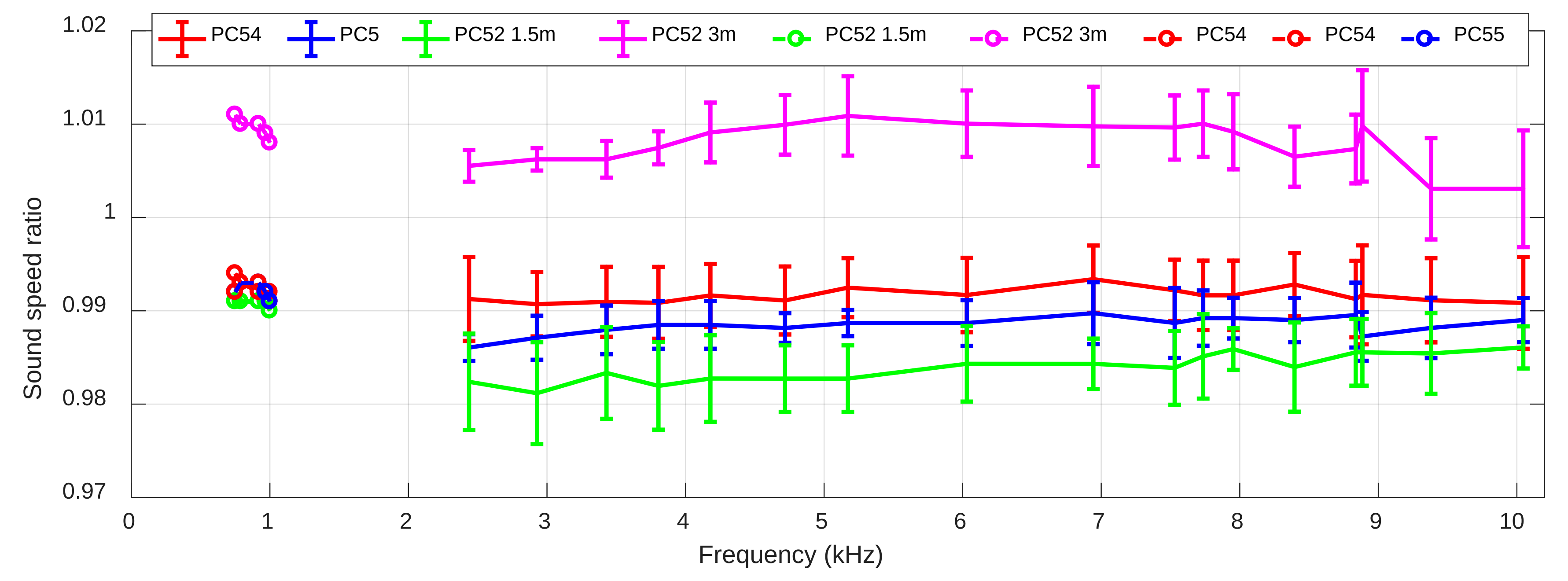

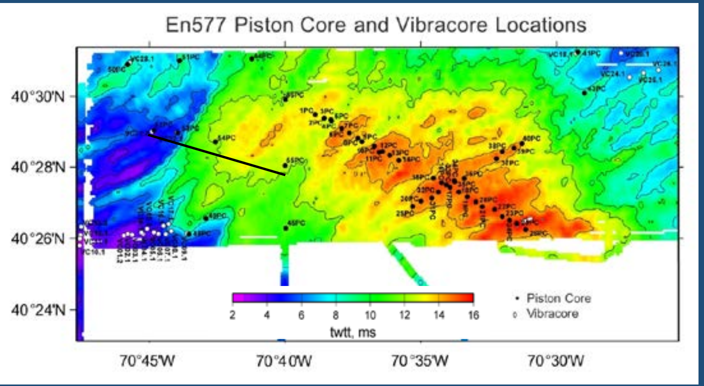

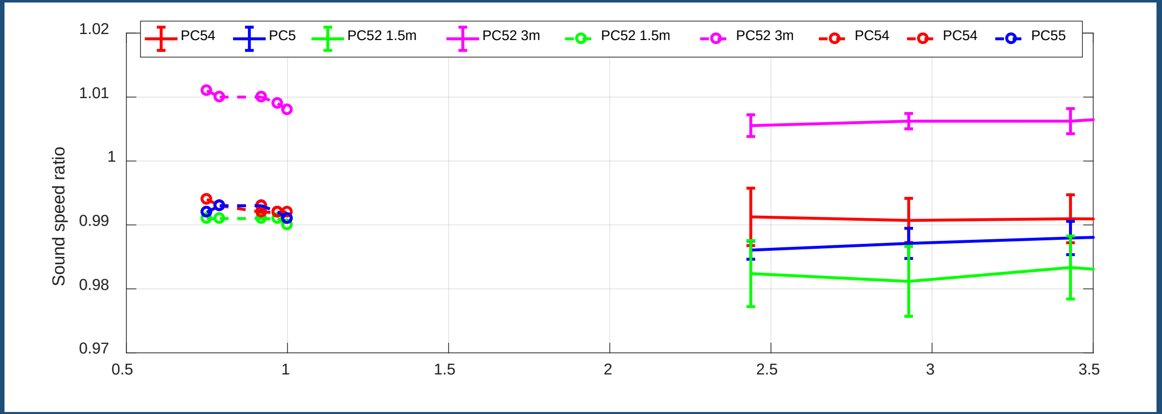

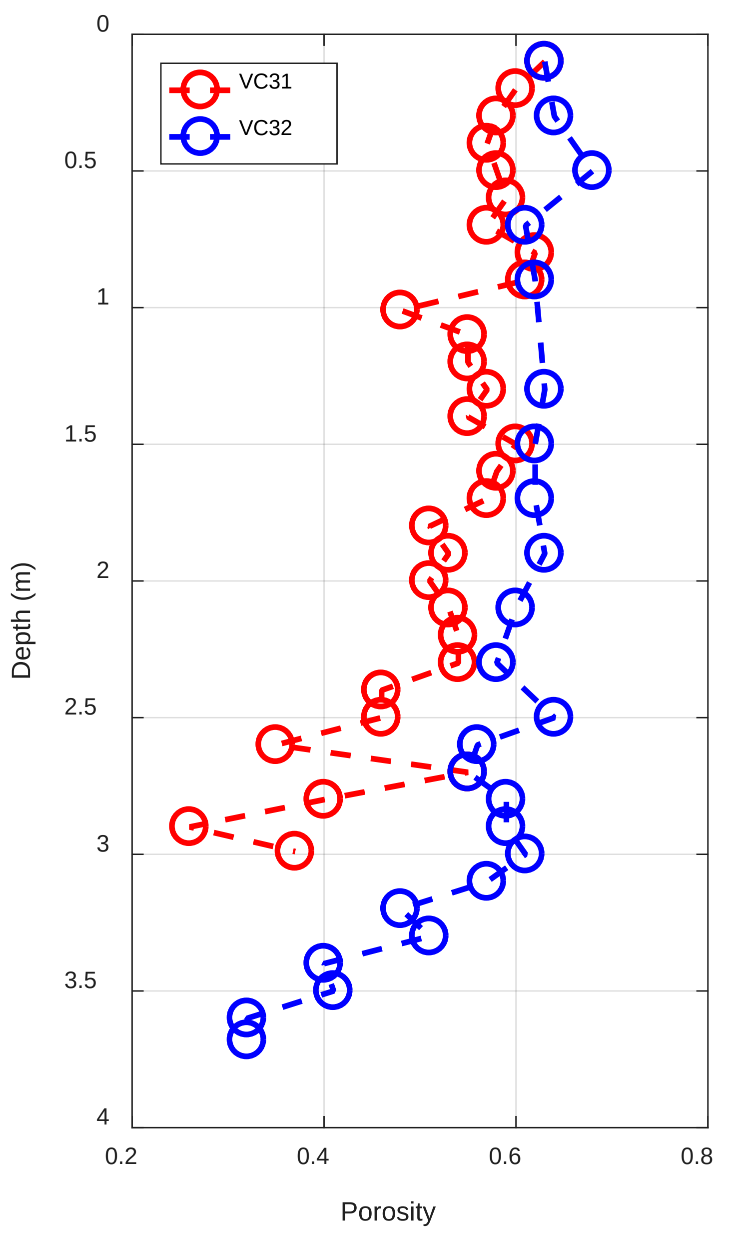
VC31
VC32
Depth (m)
0
0.5
1
1.5
2
2.5
3
3.5
4
0.2
0.4
0.6
0.8
Porosity

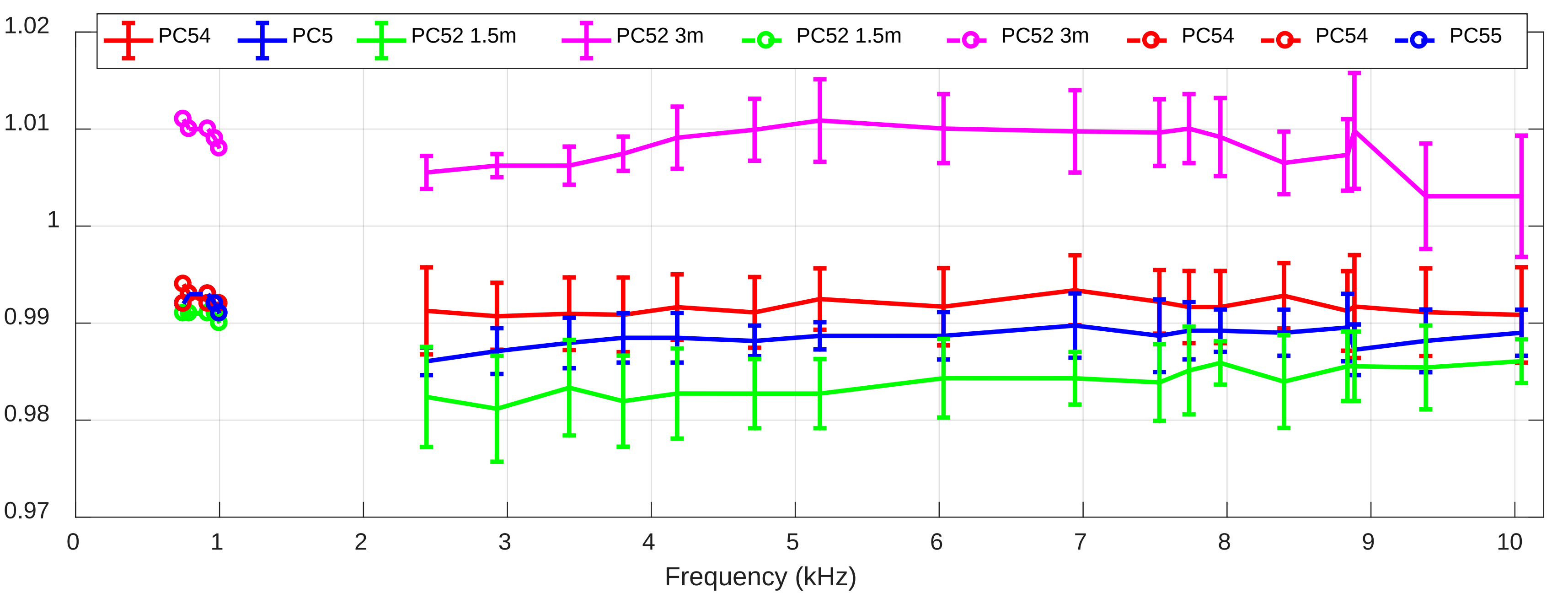
PC54
PC5
PC52 1.5m
PC52 3m
PC52 1.5m
PC52 3m
PC54
PC54
PC55
1.02
1.01
1
0.99
0.98
0.97
0
1
2
3
4
5
6
7
8
9
10
Frequency (kHz)

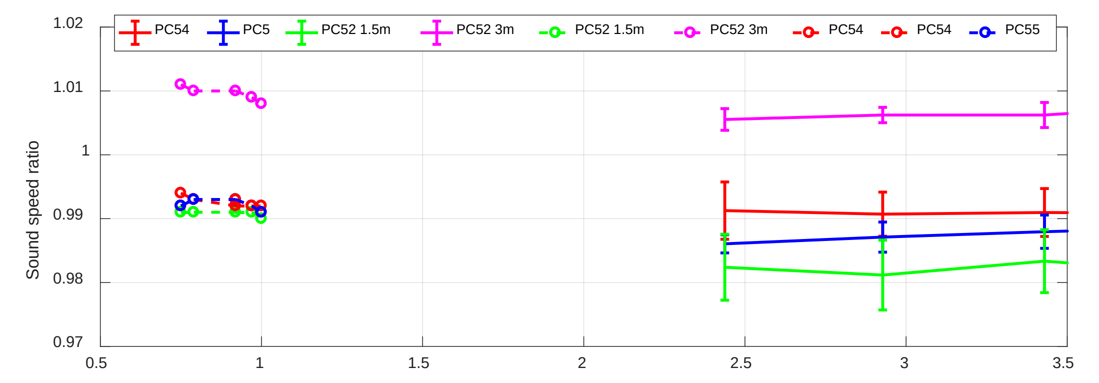
PC54
PC5
PC52 1.5m
PC52 3m
PC52 1.5m
PC52 3m
PC54
PC54
PC55
Sound speed ratio
1.02
1.01
1
0.99
0.98
0.97
0.5
1
1.5
2
2.5
3
3.5

Property variation from VC1 to VC8

- surficial mud 1.5 – 5 m
- incremental penetration for depth dependent geoacoustic properties
- Shown: data at 3 m penetration depth

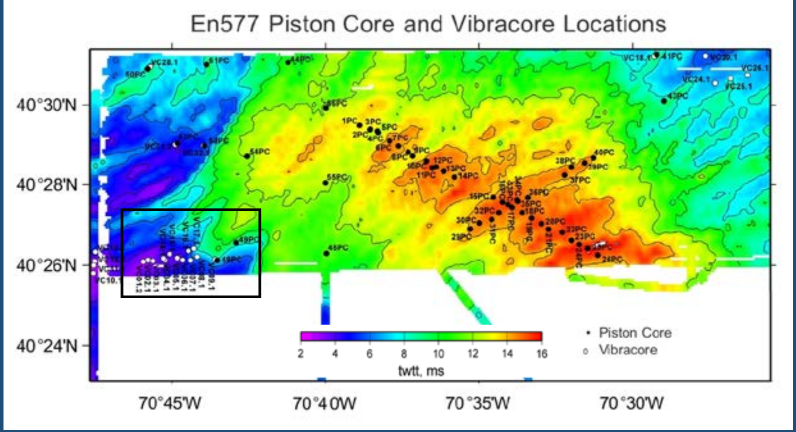

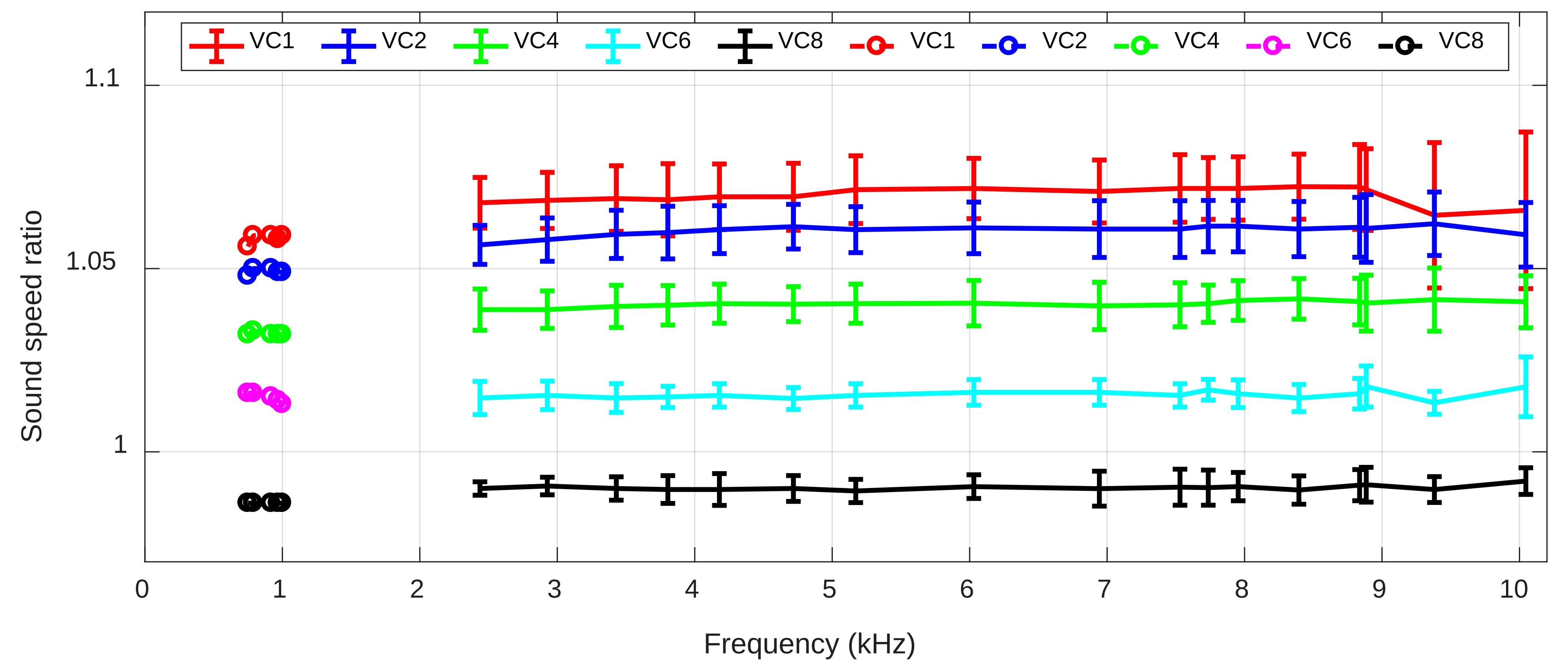

Summary and future work

- A transducer model was developed and used to model sources that are under burial conditions.
- Model generated synthetic data compare well with in-water calibration data in the frequency range of 700–1000 Hz. The procedure then was repeated for the in-sediment data.
- Thus obtained sound speed ratio compares reasonably with results obtained in the frequency range of 2 – 10 kHz, with little dispersion.

Future Work

- Measurements/modeling effort for the transducer model

Statistical Inference of Sound Speed and Attenuation Dispersion of a Fine-Grained Marine Sediment

David Paul Knobles, Christian D. Escobar-Amado, Michael J. Buckingham,
William S. Hodgkiss, *Life Member, IEEE*, Preston S. Wilson, Tracianne B. Neilsen, *Member, IEEE*,
Jie Yang, and Mohsen Badiey

***Abstract*—Acoustic recordings of signals in the 1.5–4.0-kHz band were analyzed for information about the sound speed and attenuation frequency dispersion of a fine-grained sediment found in the New England Mudpatch. Analysis of piston cores established prior bounds for a geophysical parameterization of a seabed model that predicts Kramers–Kronig dispersion relations. Sediment layers are described by the Buckingham viscous grain shearing (VGS) model that accounts for the effects of overburden pressure of compressional and shear speeds and attenuations. A statistical inverse problem was solved by using multiple samples of received levels recorded on two vertical line arrays as a function time and hydrophone depth for six frequencies in the 1.5–4.0-kHz band. A statistical inference model that assumed both model parameters and data samples are random variables quantified information content from marginalization of a conditional posterior probability distribution for the geophysical parameters that characterize the mud layer. From the inferred geophysical parameter point estimates the sediment sound speed and attenuation frequency dispersion are predicted and compared to previously reported direct measurements. Also, the predicted sound-speed gradient in the mud sediment from the VGS model is compared to a previous inference that utilized explosive sources.**

***Index Terms*—Data ensemble maximum entropy (DEME), frequency dispersion, seabed geophysical parameters.**

I. INTRODUCTION

AN IMPORTANT acoustic characteristic of a marine sediment is its frequency dependence or dispersion of the sound speed and attenuation. A goal for the Seabed Characterization Experiment 2017 was to use a combination of direct and acoustic measurements to infer the dispersion characteristics of a fine-grained sediment in the New England Mudpatch [1].

A fundamental question in remote sensing for ocean seabed characterization, such as frequency dispersion of sound speed and attenuation, is what additional information about the physical properties of the seabed not previously known or assumed known is gained from new measurments on an array of hydrophones or vector sensors. How does model complexity affect information content quantified by a conditional posterior probability distribution? Such information content can be degraded with increasing model complexity due to parameter correlations that leads to increased uncertainty [2].

This article focuses on the remote sensing of the geophysical properties of the upper portions (5 m) of a sediment composed of fine-grained materials generally possessing rigidity on the New England shelf studied by Twichell [3], Goff [4], and Chaytor [5]. Statistical inference techniques are applied to midfrequency acoustic data taken during the Seabed Characterization Experiment in 2017 to extract statistical properties of geophysical characteristics of the mud sediment from which the frequency dispersion of the sound speed and attenuation can be predicted [6]–[8]. From a Bayesian perspective, the piston core (PC) measurements made by Chaytor [5] act as *prior* information.

A complicating feature of this work is that a sediment generally has frequency dependent depth gradients of compressional and shear sound speeds and attenuations. Neglecting such gradients can bias estimates of the porosity and other parameters that are correlated with parameters such as sound speed and attenuation. The current analysis attempts to address this issue by using a new version of the viscous grain shearing (VGS) model [6]–[8] that accounts for the effects of overburden pressure through the depth effects of the compressional and shear modulus [9]. In this way, the gradients in the sound speed and attenuation are included implicitly as part of the model physics.

The rest of this article is organized as follows. Section II discusses the experimental measurements made during SBCEXP 2017. Section III discusses the geophysical model space. Section IV describes the analysis methodology that includes both a frequentist inference and a data ensemble maximum entropy (DEME) method. Section V presents the computational results and a discussion. Finally, Section VI concludes this article.

Manuscript received October 12, 2020; revised March 8, 2021 and April 26, 2021; accepted June 14, 2021. This work was supported by the Office of Naval Research Code 32, Ocean Acoustics Program under Grant N00014-20-P-2011. *(Corresponding author: David Paul Knobles.)*

Associate Editor: G. Potty.

David Paul Knobles is with Knobles Scientific and Analysis, Austin, TX 78755 USA (e-mail: dpknobles@kphysics.org).

Christian D. Escobar-Amado and Mohsen Badiey are with the University of Delaware Newark, Newark, DE 19716 USA (e-mail: christiandavide@gmail.com; badiey@udel.edu).

Michael J. Buckingham is with the Scripps Institution of Oceanography, University of California, San Diego, La Jolla, CA 92093 USA (e-mail: mjb@mpl.ucsd.edu).

William S. Hodgkiss is with the Marine Physical Laboratory, Scripps Institution of Oceanography, University of California, San Diego, La Jolla, CA 92093 USA (e-mail: whodgkiss@ucsd.edu).

Preston S. Wilson is with the Mechanical Engineering Department and Applied Research Laboratories, University of Texas, Austin, TX 78713 USA (e-mail: pswilson@mail.utexas.edu).

Tracianne B. Neilsen is with Brigham Young University, Provo, UT 84602 USA (e-mail: tbn@byu.edu).

Jie Yang is with the Applied Physics Laboratory, University of Washington Seattle, Seattle, WA 98105 USA (e-mail: jieyang@apl.washington.edu).

Digital Object Identifier 10.1109/JOE.2021.3091846

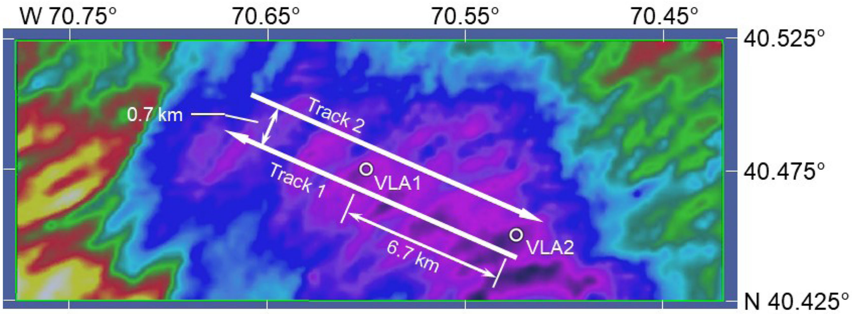

Fig. 1. *RV Endeavor* tow tracks for ITC 2015 source and VLA locations. Data samples $\mathbf{D_1}$, $\mathbf{D_2}$, and $\mathbf{D_3}$ were recorded as the towed source was moving along on Track 1, and $\mathbf{D_4}$ and $\mathbf{D_5}$ were recorded as the source was towed on Track 2.

II. Experimental Design and Measurements

The acoustic measurements of interest in this article were made on March 24 (Day 083) 2017. Fig. 1 shows the experimental configuration where the *RV Endeavor* towed a ITC 2015 transducer emitting continuous wave sound radiation at discrete frequencies at approximately 1500, 2000, 2500, 3000, 3500, and 4000 Hz. Due to the Doppler effect the center frequencies for the six tonals differ by about 5–7 Hz depending on whether the source was moving toward or away from a receiver. The source tow experiment was made along a rectangular path with the two VLA arrays placed within the rectangle. The source tracks were positioned such that they were aligned with an NW to SE orientation of the central channel of mud that defines the Mudpatch [4]. The nominal tow depth and speed were about 45 m and 3 kn, respectively. The geographical position of the Scripps Marine Physics Laboratory VLA 1 and VLA 2 were about 40 28.207° N 70 35.8266° W and 40 26.5073° N 70 31.6299° W, respectively. The two VLAs were approximately identical in that the bottom phone of each array was located at about 5 m above the water-seabed interface with a constant hydrophone spacing of 3.75 m, giving a total vertical aperture of 60 m. The water depth at both arrays was about 74.5 m.

The notation $\mathbf{D}_1$ in Fig. 1 corresponds to a data sample recorded on VLA 2 over a time interval when the source was on Track 1 and moved in an NW direction away from VLA 2. Also, $\mathbf{D}_1$ is a rectangular matrix of received levels, in dB rel 1μPa, where the rows refer to a relative time with spacing of 0.5 s and the columns refer to hydrophone channel and frequency. There are 16 hydrophones that span 60 m of the water column. The data samples are all processed such that the first time sample corresponds to the source being at the closest point of approach (CPA) on the track. For sources approaching an array, this means that the data component in time was *flipped*. For each hydrophone/channel, the levels are included at six frequencies with channel 1 in the first column, followed by channel 2, etc., for a total number of $16 \times 6 = 96$ columns. The number of row elements is 8850. At 3 kn (1.543 m/s) each data sample corresponds to the source moving a total distance of about 6800 m. $\mathbf{D}_2$ and $\mathbf{D}_3$ refer to data samples recorded on VLA 1 where the source moved toward and away from the array on Track 1, respectively. $\mathbf{D}_4$ and $\mathbf{D}_5$ refer to data samples recorded on VLA 1 where the source moved toward and away from the array on Track 2, respectively. $\mathbf{D}_6$ refers to data samples recorded on VLA 2 where the source moved toward the array on Track 2. Analysis of the $\mathbf{D}_6$ data sample, however, is beyond the scope of this article due to an inability reconcile certain signal processing criteria that apparently were a result of nonuniform motion of the source near the array. Such time periods occurred during the experiments due to the need to avoid fishing gear that was present in the area in large quantities.

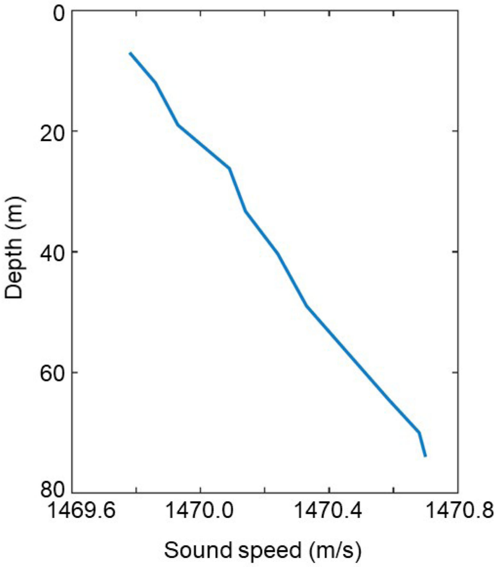

Fig. 2. SSP derived from CTD cast 03 from *RV Endeavor* on Julian day 82 hour 19, minute 12.

Fig. 2 shows a sound-speed profile (SSP) derived from CTD measurements made on *RV Endeavor* on the day that the mid-frequency acoustic data were collected. Over the course of this five-day period, warmer water slowly entered into the experimental area over the full volume of the water column causing the sound speed to slowly increase uniformly with depth. However, the sound-speed gradient was stable, about $+0.016$ 1/s. In all the computations presented in this study, the SSP was assumed fixed and was the profile that was measured closest in time to the acoustic measurements. In general, the benign properties of the water column offered a rare opportunity to apply a matched-field inversion method where the errors were dominated by seabed model mismatch as opposed to mismatch with the SSP.

A challenging aspect of the analysis was that because of marine mammal environmental regulations the duty cycle of the source was 50%, specifically 10 s on and 10 s off. To mitigate the effects of the duty cycle on the inference of information content, the data underwent a signal processing method where the peak envelopes of the received levels were extracted followed by a spline fit to the peak values. Specifically, the MATLAB function [yupper, ylower] = envelope (x, np,"peak") was utilized where yupper was chosen to return the upper envelopes of data *x* determined using spline interpolation over local maxima separated by at least np samples. By *trial and error* an optimal value of np was estimated to be about 30 for the VLA data set. The idea was to prevent a matched-field-based inversion approach from *mistaking* off-times of the source with nulls in the acoustic field that result from modal destructive interference. To be consistent, each modeled acoustic field hypothesis also underwent the same envelope processing in the evaluation of the error function [see (18)]. It was necessary to eliminate points near the start and end data and model time samples to account for the fact that spline fitting can give spuriously large values near the end points. Instead of fitting the finer details of modal interference patterns, the emphasis is the envelope structure of the field. The price to pay for stability and consistency for both model and data are a certain loss of information. It will be seen that important information gain about critical geophysical parameters can still be obtained if the sediment model chosen has an adequate balance of simplicity and physical constraints.

III. PROPOSED GEOPHYSICAL, SOURCE MOTION, AND PROPAGATION MODELS

This work considers a seabed model based on the VGS theory where each layer is characterized by N, ρ_0, ρ_g, K_0, k_g, μ_g, n, τ, and c_0, which symbolize the porosity, the wet bulk density, the grain density, the wet bulk modulus, the grain bulk modulus, the grain size, the shear hardening index, the viscous time constant, and the Wood–Mallock sound speed, respectively. The viscous time constant τ, and the strain hardening index n provide an empirical description of an effective grain-to-grain contact in the acoustic response of the sediment. Each sediment layer has its own dispersion characteristics of compressional and shear sound speed and attenuation. In addition, each layer has a depth dependence of compressional and shear speeds and attenuations and is described in [9]. The low-frequency limit of the VGS model is the sediment suspension theory described by the Wood–Mallock equations [10] and [11], with K_w and ρ_w as the bulk modulus and density of the water

$$c_0 = \sqrt{\frac{K_0}{\rho_0}} \tag{1}$$

where

$$\frac{1}{(K_0)} = \frac{N}{(K_w)} + \frac{(1-N)}{(K_g)} \tag{2}$$

and

$$\rho_0(N) = \rho_g + N(\rho_w - \rho_g). \tag{3}$$

Chaytor [5] reports that for the New England Mudpatch, the grain density of the mud is $< \rho_g > = 2500$ kg/m^3, which is consistent with the value of 2499 kg/m^3 inferred in [12] that employed SUS explosive charges to estimate a low-frequency geoacoustic profile for the Mudpatch. Assuming a value for ρ_w of 1030 kg/m^3, (3) provides a linear relationship for $\rho_0(N)$. Following Buckingham [8], an expression for grain size is

$$\mu_g(N) = \frac{2\Delta(2B-1)}{1-B} \tag{4}$$

where

$$B = \left(\frac{1-N}{1-N_{\text{min}}}\right)^{1/3} \tag{5}$$

with $N_{\text{min}} = 0.37$. The roughness parameter is defined as $\Delta = 1\ \mu\text{m}$ [13]. In units of Krumbein ϕ scale [14], the grain size can be expressed as

$$\phi = -\log_2(\mu_g/\mu_0) \tag{6}$$

where $\mu_0 = 1000\ \mu$m.

The basic geophysical parameters for the mud sediment and the deeper layers are shown in Table I. Parameter values are either fixed or have upper and lower bounds that define a search space. Between the upper and lower bounds, it is assumed that the prior probability distribution is uniform. Chaytor's analysis [5] suggests that the upper portion of the mud is a mixture of about 30% sand, 50% silt, and 20% clay. The sediment composition changes to 10%–20% sand, 60% silt, and 10% clay below about 2 m. Additional parameters include the compressional modulus, the shear modulus, the shear coefficient, and the grain shearing coefficient, all of which are held fixed based on the work by Buckingham [8] and Richardson [13]. The remainder of the layers are assumed fixed from previous results. Each layer has a depth dependence due to overburden pressure; this dependence is specified by the depth dependence of the compressional and shear modulus and is described in [9]. The resulting depth dependence for both the compressional and shear sound speeds and attenuations generally vary with frequency and nonlinearly with depth. At every depth, the compressional speed and attenuation satisfy a Kramers–Kronig dispersion relationship [15]–[17].

The VGS theory was originally derived in connection with coarser sediments, the sands and silts, in which the grains are roughly spherical in shape. It has been found, however that the VGS dispersion relations provide a reasonable representation of the wave speeds and attenuations, not only in sands but also in the finer-grained materials, such as the clays and muds. Many of the mineral particles found in mud are far from spherical, taking the form of high-aspect-ratio needles or platelets, which raises the question as to why VGS matches the fine-grain dispersion data so well? It has been argued in [9] that the geometrical shapes of the particles are immaterial, the important factor in VGS being the detailed nature of the contact between one particle and another. In the context of such a contact, the point of a needle is much the same as a sphere with the same radius of curvature. More details are given in [9], but the essential conclusion, which is supported by experimental evidence, is that the VGS theory has application to compressional waves and shear waves in a wide range of

TABLE I
GEOPHYSICAL PARAMETERS FOR MULTILAYERED REPRESENTATION OF SEABED

Parameter, symbol,	Mud	T_1	T_2	T_3	S	units
Content, –	clayey silt	sand-silt-clay	sand-silt-clay	sand-silt-clay	fine to medium sand	–
Layer thickness, LT	9.3	1.0	1.0	1.0	5.0	m
Porosity, N	[0.563 –0.640]	0.563	0.52	0.50	0.40	—
Bulk density, ρ_0	Eq. 3	1645	1648	1700	1963	$\frac{kg}{m^3}$
Grain density, ρ_g	2500	Eq. 3	Eq. 3	Eq. 3	Eq. 3	$\frac{kg}{m^3}$
Mean grain diameter, μ_g	Eqs. 4-6	Eqs. 4-6	Eqs. 4-6	Eqs. 4-6	Eqs. 4-6	ϕ
Mineral grain bulk modulus, K_g	[13.5–15.5]	15	30	32	32	GPa
Sediment bulk modulus, K_0	Eq. 2	Eq. 2	Eq. 2	Eq. 2	Eq. 2	GPa
Woods Mallock sound speed, c_0	Eq. 1	Eq. 1	Eq. 1	Eq. 1	Eq. 1	m/s
Compressional modulus, γ_p	7.01E07	7.01E07	7.01E07	7.01E07	7.01E07	Pa
Shear modulus, γ_s	1.75E06	1.75E06	1.75E06	1.75E06	1.75E06	Pa
Strain hardening index, n	[0.01–0.1]	0.05	0.0384	0.08854	0.08854	—
Visco-elastic time constant, τ	∞	0.01	0.0012	0.00012	0.00012	s
Compressional coefficient, γ_{p0}	3.54E08	3.54E08	3.54E08	3.54E08	3.54E08	Pa
Shear coefficient, γ_{s0}	4.47E07	4.47E07	4.47E07	4.47E07	4.47E07	Pa
Grain shearing coefficient, Ξ	0.022	0.022	0.022	0.022	0.022	Pa

The parameters in bold face for the mud layer along with the speed of the source are those that form the hypothesis space.

sediments, from coarse sands to fine grained muds and clays, making it an appropriate choice for representing the stratified sediment at the New England Mudpatch.

Three parameters in the mud layer are viewed as unknown or random, and in Table I, the lower and upper parameter bounds are presented in brackets. The upper and lower bounds for N were provided by Chaytor [5]. The upper and lower bounds for n are based on values reported by Buckingham [8]. Buckhingham has noted that a significant amount of data can be explained by setting n to be 0.0866. Generally, smaller values of n are indicative of a softer sediment. Since the mud sediment is reportedly a mixture of clays, silts, and sands, n is allowed to vary between 0.01 and 0.10. The upper and lower bounds for the grain bulk modulus for the mud were reported by Chaytor [5]. The remainder parameters in the mud layer are assumed known. For example, it was decided to fix the value of τ to infinity because [1] suggested that to first order there was only a small degree of frequency dispersion of the sound-speed ratio (SSR) in the 100–100 000-Hz band. Most specifically, there does not appear strong evidence of a transition frequency that would be proportional to the inverse of τ. It is of interest to note that in the limit that τ goes to infinity, the VGS theory reduces to the original grain shearing model.

The sediment characterization of layers beneath the fixed mud layer are based on previous results. For example, Twichell [3], Goff [4], and Chaytor [5] report on the existence of a *transition layer* from the mud to the sand layer. The transition layer has been reported to have a thickness of 2–3 m. In this work, we fixed this layer thickness at 3 m, but made the layer have a more continuous transition by dividing it into three 1 m layers with decreasing porosity. Namely, a depth gradient of the physical parameters was introduced for the sediment to vary from mud to sand. The transition layer has also been inferred from the analyses of acoustic data (see, for example, [18] and [19]) using trans-dimensional Bayesian inversion processing. The assumed properties of the sand layer are based mostly on finding porosity values that, when used in the VGS model would predict the reported sound speeds by Yang [20]. No attempt at inverting for parameters in these deeper layers was made because due to the lack of information content in the 1.5–4.0-kHz band and at the long ranges. In other words, the acoustic field that penetrated into the seabed in the 1.5–4.0-kHz band was for the most part confined to the first 5 m or so of the mud.

In the simple case of uniform source motion (assumed in this article), $\mathcal{X}_s(t)$ is represented by a straight line or track that has a closest position of approach (CPA) range (r_{cpa}) to a VLA. At any point on this track, the distance or range from the source to the receiver r is

$$r(t) = \sqrt{(r_{\text{cpa}})^2 + (\mathcal{X}_s(t))^2} \tag{7}$$

where

$$\mathcal{X}_s(t) = \mathcal{X}_s(t=0) + St \tag{8}$$

and S is the speed of *RV Endeavor*. The reported source depth was 45 m and is held fixed. In this study, the CPA range is assumed fixed, but the speed is viewed as a random parameter with upper and lower bounds of 2.8 and 3.3 kn, respectively.

For each sampling of the hypothesis space, the frequency and depth-dependent sound speeds and attenuations computed with the VGS model along with source parameters are then input into a broadband elastic normal mode algorithm [21]. The resulting received pressure field $\mathcal{P}$ in cylindrical coordinates is then computed as

$$\mathcal{P}(f, z, r) = 10^{\text{SL}/20} * \mathcal{G} \tag{9}$$

where $\mathcal{G}$ is the complex Green's function solution to the Helmholtz equation for a unit point source

$$\mathcal{G}(f, z_s, z, r) = \frac{i}{4\rho(z_s)} \sum_m \phi_m(z_s)\phi_m(z) H_0^1(k_m r) \tag{10}$$

where k_m and ϕ_m are the horizontal wave number eigenvalues and depth dependent eigenfunctions, respectively. SL(f) are the source levels and are assumed fixed from measurement (deterministic).

IV. STATISTICAL INFERENCE METHODS

The following two procedures of analyses are considered: a *frequentist* methodology and a DEME approach.

A. Frequentist Statistics

Frequentist statistics [22] are based on an estimate $\mathbf{\Theta}_{\text{est}}$ of a vector of parameter values from multiple measurements, and then using this estimate when making all predictions of, for example, the received acoustic level RL$(\mathbf{\Theta}_{\text{est}})$. The notation used in this discussion is that $\mathbf{\Theta}$ is a vector with components $(\Theta_1, \Theta_2, \ldots \Theta_{K-1}, \Theta_K)$. Frequentists assume that the true value $\mathbf{\Theta}_{\text{true}}$ is fixed (deterministic) but unknown, and that $\mathbf{\Theta}_{\text{est}}$ is a *reasonable* approximation to $\mathbf{\Theta}_{\text{true}}$. However, it is assumed that the data $(\mathbf{D}_1, \mathbf{D}_2, \ldots \mathbf{D}_{M-1}, \mathbf{D}_M)$ are not fixed, but are random. In the frequentist method, a point estimate is the single best parameter value estimate of $\hat{\mathbf{\Theta}}_{\text{true}}$ found by minimizing an error function, $E(\mathbf{\Theta}, \mathbf{D}_m)$. Mathematically this idea is expressed as

$$\hat{\mathbf{\Theta}}_m = \text{Argmin}_{\mathbf{\Theta}}\ E(\mathbf{\Theta}_m, \mathbf{D}_m), \quad m = 1, 2, \ldots, M. \tag{11}$$

This point estimate is a random variable because the data sample is a random selection from a probability distribution of samples. The main problem with such a point estimate based on a single data sample is that there is no uncertainty. However, multiple data sets do allow one to find an average and a standard deviation for each parameter, even though an individual result has no uncertainty. This is fully analogous to rolling dice.

B. Data and Environmental Ensemble Maximum Entropy Statistics

The DEME method as implemented by Knobles *et al.* [12], [23], [24] in remote sensing applications in ocean acoustics has its origins with the early works of Cox [2], Kullback [25], Jaynes [26]–[27], and Bilbro [28] that demonstrated the connectivity of machine learning and maximum entropy. A question that arises for DEME is how many data samples can be in the data resemble before the addition of a new sample gives no additional information other than the statistic. When the size of the data ensemble space reaches this size, one can say that statistical sufficiency has been reached. For a reference on information and sufficiency the reader is also referred to Jayne's classic book on probability theory [29].

Before making a comment on DEME, it is useful to point out the differences between frequentist and Bayesian concepts in probability theory. Instead of using only $\hat{\mathbf{\Theta}}$ to make predictions, a Bayesian approach considers all possible values of $\mathbf{\Theta}$ to compute a probability distribution to ascertain the degree of certainty for various $\mathbf{\Theta}$ values. Also, in contrast to a frequentist approach the parameters in $\mathbf{\Theta}$ are nondeterministic and, thus, represented as random variables. Furthermore, in a Bayesian method, the data are fixed, namely, the data are deterministic. The goal of the Bayesian model is to quantify questions about information content and sufficiency. For example, the Bayesian concept quantifies the information that the data contain that the prior information did not? It also addresses how much parameter correlations [2] contribute to the uncertainty for a given parameter.

To be consistent in the analysis of remote sensing data, both the data and the model parameters should be treated as nondeterministic. This is the essence of DEME [12], [23], [24] whose goal, such as a Bayesian method, is to construct a conditional posterior probability distribution $P(\mathbf{\Theta}_m|\mathbf{D}_m)$ for $m = 1, 2, \ldots M$ from which marginal probability distributions can be computed. One can then average the marginal distributions over the data samples to obtain a more realistic assessment of the uncertainty of the parameter inference. The conditional marginal distribution for the parameter θ_k and data sample $\mathbf{D}_m$ is

$$P_m(\theta_k|\mathbf{D}_m) = \int d\theta_1 d\theta_2 \cdots d\theta_{k-1} d\theta_{k+1} \cdots d\theta_M P(\mathbf{\Theta}|\mathbf{D_m}) \tag{12}$$

with

$$P(\theta_k|\mathbf{D}_m) = P(\theta_k)\frac{\exp[-\beta_m \mathcal{E}_m(\theta_k, \mathbf{D}_m)]}{Z_m} \tag{13}$$

where $\mathcal{E}_m$ is an error function. Z_m and β_m are analogous to the partition function and the Boltzmann factor, respectively, with

$$Z(\beta_m) = \int dH P(H) \exp[-\beta_m \mathcal{E}_m(\theta_k, \mathbf{D}_m)] \tag{14}$$

and where β_m is determined by solving a constraint integral equation.

From the marginals, we can, for example, find the expectation of θ from the distributions

$$E_m(\theta_k) = \int d\theta_k\ \theta_k P_m(\theta_k|\mathbf{D}_m). \tag{15}$$

One can also define an average marginal distribution

$$< P(\theta_k) >= \frac{1}{M}\sum_m P_m(\theta_k|\mathbf{D}_m) \tag{16}$$

from which

$$E(\theta_k) = \int d\theta_k\ \theta_k\ < P(\theta_k) > . \tag{17}$$

Finally, the error function utilized in the construction of the posterior distribution is a squared error

$$\mathcal{E}(\mathbf{\Theta}, \mathbf{D}) = \sum_{\mathbf{i}}\sum_{\mathbf{j}}\sum_{\mathbf{k}} (\mathbf{D}(\mathbf{f_i}, \mathbf{z_j}, \mathbf{r_k}) - \mathcal{D}_{\mathbf{s}}(\mathbf{f_i}, \mathbf{z_j}, \mathbf{r_k}))^{\mathbf{2}} \tag{18}$$

where

$$\mathcal{D}_s = 20\ \log_{10}|\mathcal{P}(f, z, r)| \tag{19}$$

where $\mathcal{P}(f, z, r)$ is given in (9) and (10) and f_i, z_j, r_k represent frequency, receiver depth, and source–receiver range (7).

TABLE II
$\hat{\theta}_j$ FOUND VIA MONTE CARLO METHOD WITH 200 000 SAMPLES OF Θ

Data sample	N	n	k_g (Pa)	S(knots)	$E(\hat{\theta}_n)$ (dB^2)
1	0.5959	0.0627	1.4442x10^{10}	3.341	1.42x10^{7}
2	0.5881	0.0611	1.4444x10^{10}	3.175	1.36x10^{7}
3	0.5763	0.0471	1.4479x10^{10}	3.197	1.47x10^{7}
4	0.6274	0.0599	1.3580x10^{10}	3.096	1.29x10^{7}
5	0.5817	0.0476	1.4852x10^{10}	3.241	1.48x10^{7}
mean	0.59388	0.05568	1.44x10^{10}	3.21	—
std	0.01799	0.00686	4.19x10^{8}	0.08	—

TABLE III
$E_m(\theta_k)$ FOR $m = 1, 2, \ldots, M$ AND $E(\theta_k)$ AND STANDARD DEVIATIONS

Data sample	N	n	k_g (Pa)	S (knots)
1	0.6026 ± .014	0.0658 ± .012	1.4508x10^{10} ± 6.21698x10^{8}	3.2837 ± 0.1792
2	0.5892 ± .0153	0.0599 ± .0182	1.4481x10^{10} ± 6.0823x10^{8}	3.1596 ± 0.1729
3	0.5829 ± .0119	0.0614 ± .0213	1.4543x10^{10} ± 6.1x10^{8}	3.2619 ± 0.1338
4	0.6086 ± .0166	0.0684 ± .0201	1.441x10^{10} ± 6.2778x10^{8}	3.2598 ± 0.133
5	0.5826 ± .012	0.05818 ± .0201	1.4543x10^{10} ± 6.0108x10^{8}	3.2773 ± 0.1294
mean of $< P(\theta_k) >$	0.59318	0.064	1.45x10^{10}	3.28
std relative to mean	0.01058	0.003658	5.122x10^{7}	0.044

V. SCIENTIFIC FINDINGS

The five data samples from the midfrequency towed source recorded on the VLAs are used to estimate four parameters. The full parameter space consists of

$$\boldsymbol{\Theta} = (N, n, k_g, S) \tag{20}$$

where S is the speed of the source. The CPA ranges are held fixed at the measured value provided by global positioning measurements and are 364, 378, 378, 324, and 324 m for the collection of samples $\mathbf{D}_1$, $\mathbf{D}_2$, $\mathbf{D}_3$, $\mathbf{D}_4$, and $\mathbf{D}_5$, respectively.

The following four point estimates are computed to generate modeled transmission loss that can be compared to measured TL.

1) Optimal inversion solution $\hat{\boldsymbol{\Theta}}_m$, $m = 1, 2, \ldots, M$.

2) Frequentist average of $\hat{\boldsymbol{\Theta}}_m$ over data samples, via Monte Carlo sampling shown in Table II

$$< \boldsymbol{\Theta} > = \frac{\mathbf{1}}{\mathbf{M}} \sum_{\mathbf{m}} \hat{\boldsymbol{\Theta}}_{\mathbf{m}}. \tag{21}$$

3) Expectation of parameters from marginals $P_m(\theta_k|\mathbf{D}_m)$ for $m = 1, 2, \ldots, M$ (15) shown in Table III

$$E_m(\theta_k) = \int d\theta_k \; \theta_k P_m(\theta_k|\mathbf{D}_m). \tag{22}$$

4) Expectation from ensemble averaged marginals (17) shown in Table III

$$E(\theta_k) = \int d\theta_k \; \theta_k \;\; < P(\theta_k) > . \tag{23}$$

Table II shows the frequentist results for the point estimates that correspond to the optimized results for $\mathbf{D_m}$; $m = 1, \ldots, 5$. The optimal solutions $\hat{\boldsymbol{\Theta}}_m$ were found with Monte Carlo sampling of the hypothesis space. It was generally found that 200 000 random samples of $\hat{\boldsymbol{\Theta}}_m$ was sufficient in finding $\hat{\boldsymbol{\Theta}}_m$. A problem with a frequentist prediction is that it cannot address the question of whether the number of data samples provided additional information mentioned above that provided by the priors.

Fig. 3 shows the marginal probability distributions $P_m(\theta_k|\mathbf{D}_m)$ $m = 1, 2, \ldots, 5$ using the DEME method. With the exception of $P_4(\theta_k|\mathbf{D}_4)$, the distributions for N, n, and S are single-peaked with a modicum degree of symmetry, while the distributions for k_g are essentially flat. Relative to the uniform prior distributions information was clearly gained for N, n, and S while essentially no information was gained for k_g. $P_4(\theta_k|\mathbf{D}_4)$ has distributions for N and n that have a non-Gaussian form. Fig. 3 also shows the distributions for the average distributions $< P(\theta_k) >$. The fact that the average marginal distributions are also generally peaked demonstrates that the standard deviations of the marginals are small and do not have a large off-set for different data sample m values. This is suggestive that for at least $P_m; j = 1, 2, 3, 5$ the data samples belong to the same statistical distribution, which in turn suggests that the mud variability in the area of the tow track rectangle in Fig. 1 is generally small.

Table III shows the statistic results for the point estimates that correspond to the average values from the marginal distributions. There is good agreement between the optimized results in Table II and the average results in Table III. However, an important point is that one would not have known if the point estimates

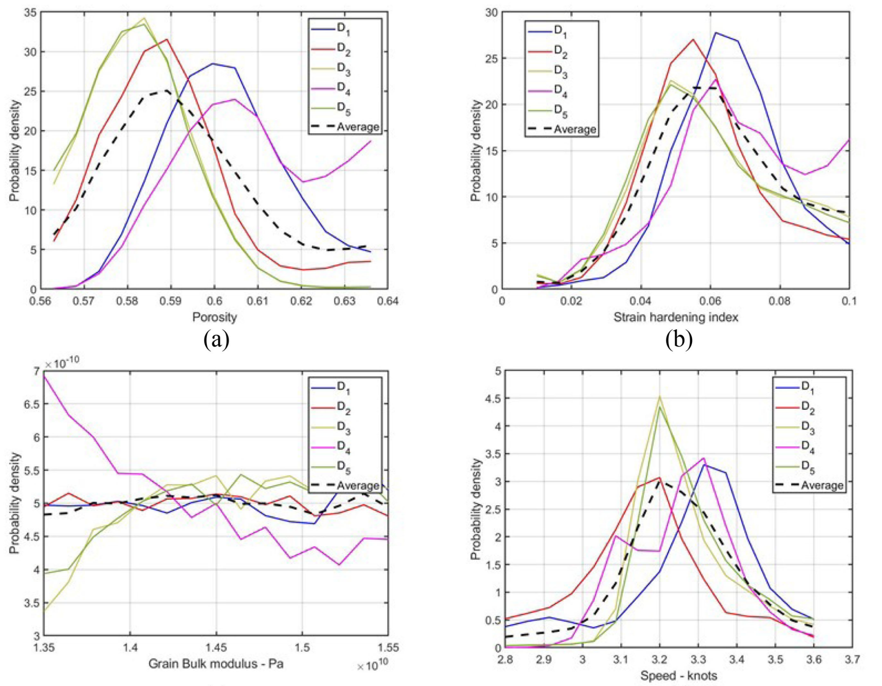

(a) (b) (c) (d)

Fig. 3. Marginal distributions $P_m(\theta_k|D_m)$ for (a) N, (b) n, (c) k_g, and (d) S for $j = 1, 2, 3, 4,$ and 5 and average distributions.

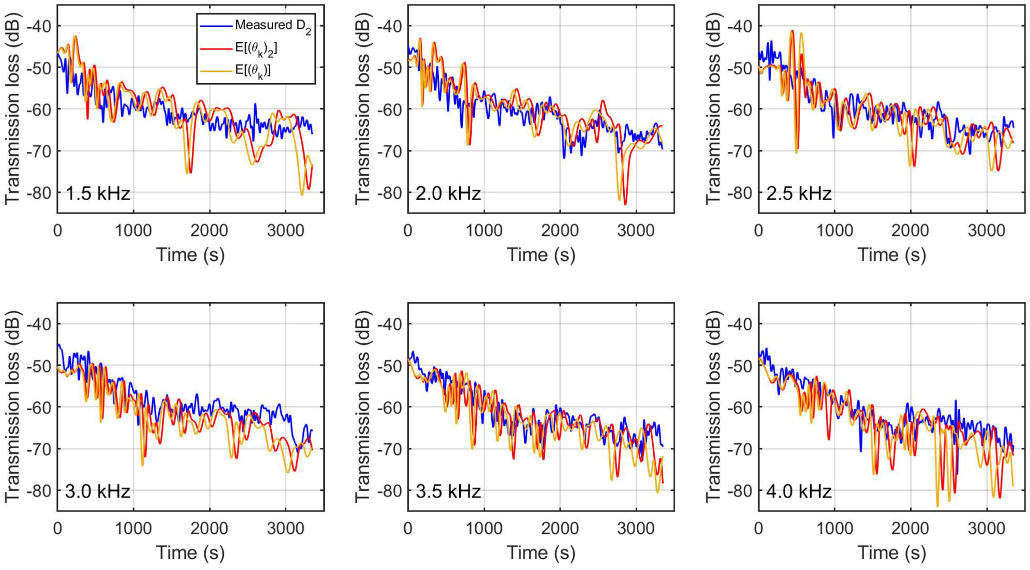

Fig. 4. Comparison of and measured TL for $\mathbf{D_2}$ on hydrophone 16 with modeled TL using parameter expectation values $E_2[(\theta_k)]$ and $E[\theta_k)]$.

that used the optimal results (see Table II) made sense unless the DEME computations that provided the estimates based on the marginal distributions in Fig. 3 had been made.

Fig. 4 shows the data-model comparisons for the transmission loss (TL = RL − SL) as a function of time for the six tonal frequencies using the $\mathbf{D_2}$ on hydrophone 16 with modeled TL using parameter expectation values $E_2[(\theta_k)]$ and $E[(\theta_k)]$. The difference in the two modeled solutions is small, and overall there is qualitative agreement between the modeled solutions and the measured TL.

Fig. 5 is the same as Fig. 4 except that the two modeled solutions are $E_4[(\theta_k)]$ and $E[(\theta_k)]$. There are larger difference between the modeled solutions $E_4[(\theta_k)]$ and $E[(\theta_k)]$. The larger differences may be ascribed to the previous observation in Fig. 3 that of the five data samples, the marginals produced had non-Gaussian attributes, and thus, $E_4[(\theta_k)]$ and $E[(\theta_k)]$ have larger differences.

Fig. 6 shows the predicted sediment depth-dependent compressional and shear sound speed and attenuation for the $E(\theta_k)$ VGS parameter values in Table III. For the compressional sound

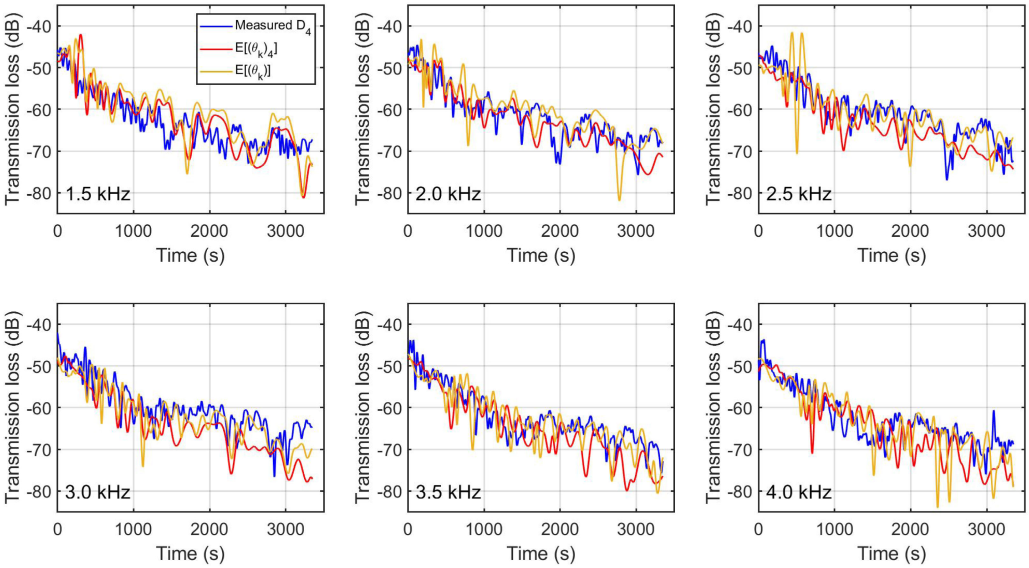

Fig. 5. Comparison of and measured TL for $\mathbf{D_4}$ on hydrophone 16 with modeled TL using parameter expectation values $E_4[(\theta_k)]$ and $E[\theta_k)]$.

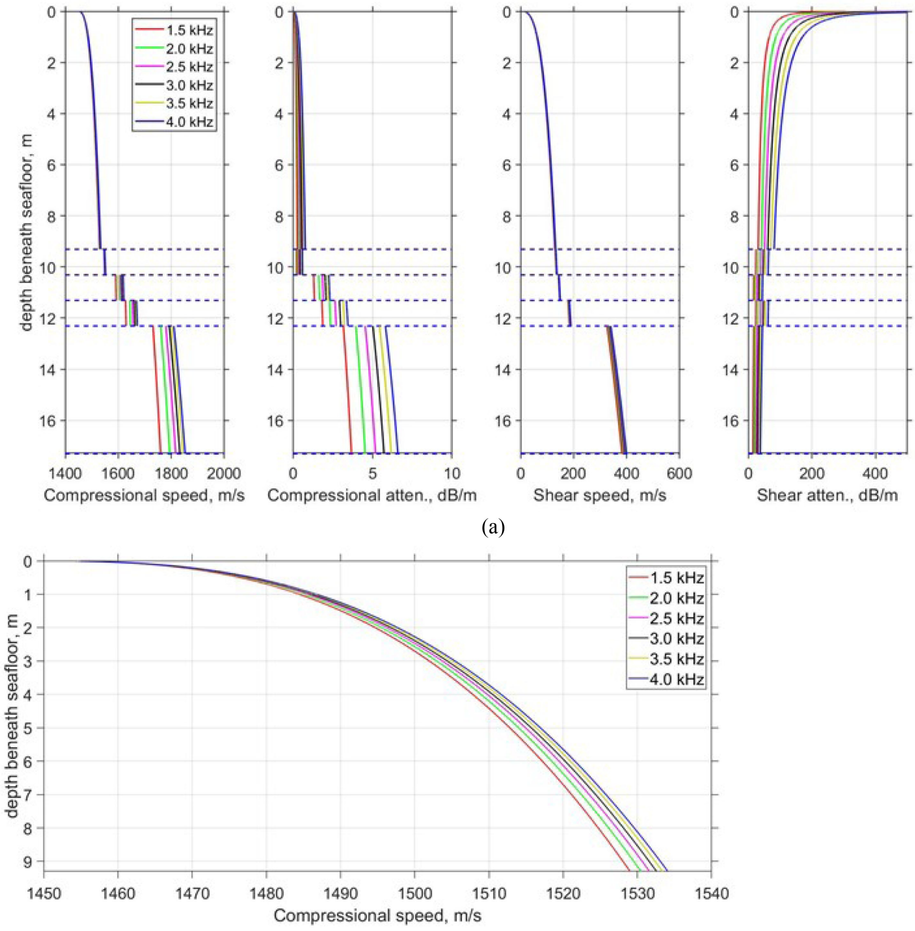

Fig. 6. Predicted depth dependence of mud sediment parameters with VGS theory. (a) Compressional sound speed, compressional attenuation, shear sound speed, and shear attenuation. (b) High resolution of compressional sound speed.

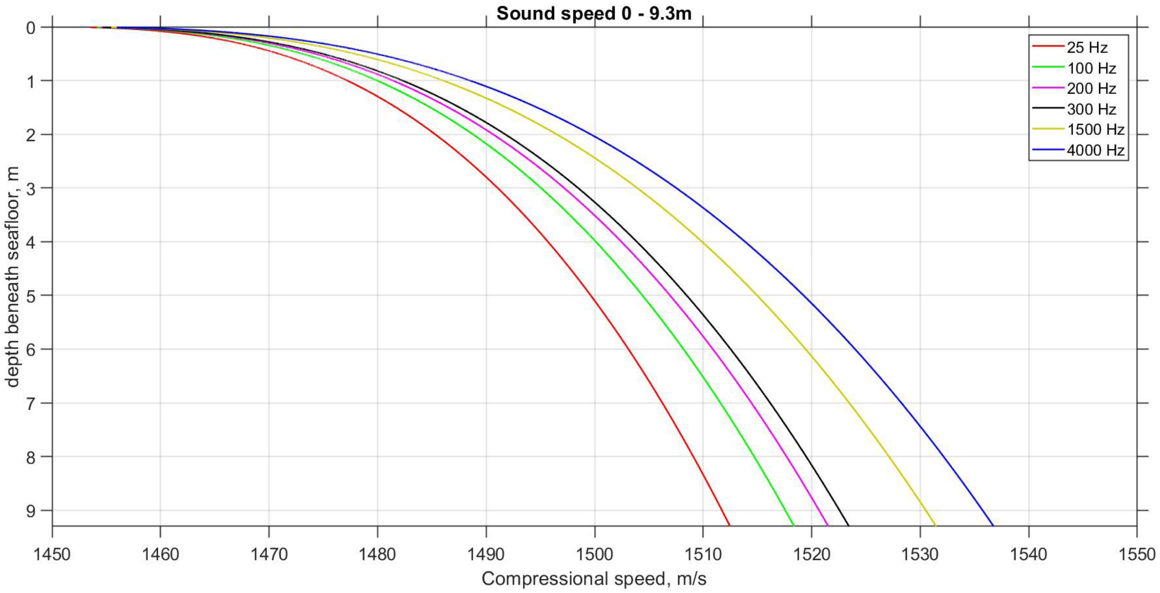

Fig. 7. Predicted depth dependence of mud sediment compressional sound speed versus depth in the 25–4000-Hz band.

speed, there is little frequency dispersion in the 1500–4000-Hz band. However, the sound-speed gradient has a strong nonlinear depth dependence. For example, in the depth interval 0–2 m, the sound speed changes from about 1456 m/s to about 1498 m/s. This gives an average gradient of about 21 (1/s). From 2 to 9.3 m, the sound speed changes from 1498 m/s to about 1535 m/s, for an average gradient of about 5.1 (1/s). The average gradient over the 9.3 m layer of the mud is about 8.5 (1/s).

Fig. 7 shows an extension of the bandwidth to the 25–4000-Hz band for the compressional sound speed versus depth using the VGS model. One observes that the predicted sound-speed gradient decreases as the frequency decreases. In the 25–300-Hz band, the average gradient is about 7.1 1/s. In [12], an effective linear gradient for the mud was found to be about 9.5 1/s from SUS data processed in the 25–275-Hz band. Thus, the VGS model with the inclusion of the overburden pressure terms in the compressional and shear modulus provides a possible effective linear gradient.

Fig. 8 shows the predicted SSR and attenuation dispersion predictions based on the mean of $< P(\theta_k) >$ and standard deviations of the porosity N, the strain hardening index n, and the grain bulk density k_g presented in Table III. For these three parameters, we considered the mean of the cumulative distribution, the mean plus the standard deviation, and the mean minus the standard deviation for a total of 27 VGS parameterizations. Then, using these 27 parameterizations the VGS model was utilized to compute the dispersion of the compressional SSR and the attenuation. SSR is the ratio of the compressional sound speed at the surface of the sediment to the sound speed at the bottom of the water column. The span of these curves provides an estimate of the uncertainty for both the SSR and the attenuation. Direct measurements of the sound speed reported by Yang and Jackson [20] in the 2–10-kHz band and by Ballard [30] in the 25–200-kHz band are included in Fig. 8, along with a included is a low-frequency estimate inferred from an analysis of SUS explosive charges in the 25–275-Hz band [12]. The black box represents direct sound speed measurements made at five locations that span the area around VLA 1 and VLA 2 [20]. The box attempts to show the range of values reported at the different locations where the sediment acoustics speed measurement system (SAMS) was deployed in Mudpatch. The relevant measurements reported in [20] were approximately between VLA 1 and VLA 2, which are close to PC 16 and PC 18 that were collected by Chaytor [5], respectively. Yang and Jackson [20] measured near PC 16 a ratio of about 0.996 and to the SE at PC 18 measured a value of 0.999 in the 2–10-kHz band. The prediction in Fig. 8 is 0.996 at 4 kHz and, thus, is in agreement with [20]. With the exception of the acoustic core measurement at 25 kHz, the measurements of the SSR reported by Ballard [30] lie within the statistical predictions of the VGS model.

The VGS dispersion curve for the SSR is aligned with the coring estimates above 1.5 kHz but shows greater SSR than previously estimated at the lower frequecies. The SSR reported in [12] in the 25–275-Hz band was 0.9775, which falls below the dispersion curves that were inferred in the 1.5–4.0-kHz band. This low-frequency inference did not use a seabed physics model and instead inverted directly for the SSR and a linear gradient. The attenuation was assumed to be about 0.01 dB/m at 1 kHz with an exponent of unity. It is difficult to understand the difference. Whether the VGS model has difficulties at the low frequencies or setting $\tau = \infty$ is not completely correct for the lower frequencies for a mud sediment is an open question.

Finally, Fig. 8 shows the predicted attenuation dispersion curves for the 27 parameterizations, which shows that the mean attenuation is about 0.045 dB/m at 1 kHz using the ensemble average parameter values.

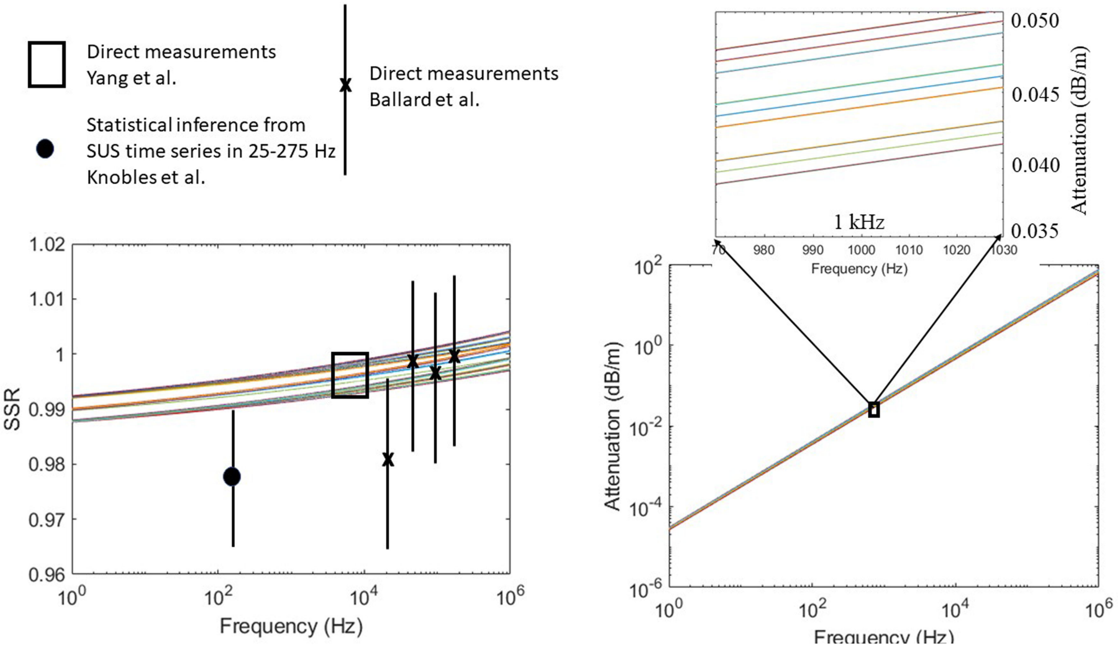

Fig. 8. Predicted SSR and attenuation derived from ITC2015 source data with VGS model compared to direct measurements and the low-frequency estimate in [12]. The 27 smooth curves are those predicted by the VGS model using the average value and standard deviations of N, n, and k_g, which allows for an inference of the uncertainty of the SSR and attenuation.

VI. CONCLUSION

The predicted dispersion of the SSR in Fig. 8 using two statistical measures and the VGS model are consistent with the direct measurements made by Yang and Jackson with the seabed acoustics measurements system (SAMS). The unique feature of this sediment is that its SSR is generally less than unity with a very weak frequency dependence of the sound speed over a large bandwidth. An important point is that the VGS predictions for the SSR and the attenuation obey a Kramers–Kronig dispersion relationship. The inclusion of this important principle of physics removes nonphysical parameter estimates for sound speed and attenuation that in turn can lead to erroneous sonar predictions.

The analysis suggests that the five data samples analyzed belong to the same statistical distribution, which in turn suggests that the mud variability in the area of the tow track rectangle around the two VLAs is generally small. From the TL data-model comparisons, both the average frequentist and the ensemble-averaged $E(\theta_k)$ solutions generally produce TL predictions that qualitatively match the measured data. The marginal distributions for the porosity N and strain hardening index n are single peaked functions and have only a small degree of skewness. While the distributions for k_g are generally flat in the assumed prior bounds, they do not appear to cause significant uncertainty in N and n. These observations are consistent with the small difference in the predicted sound speed and attenuation dispersion using these two statistical measures.

While the frequentist predictions compare well with those provided by the DEME, one cannot know *a priori* how many data samples are required to produce results that are in agreement. For the Mudpatch experiment, the measurements were made when the water column was near isospeed. During the warmer months when the water column is stratified and has a larger random component, one can expect the number of data samples required to achieve a similar parameter uncertainty will increase.

Challenges in this work included the fact that the moving source had a 50% duty cycle which, left unaddressed, would allow the inversion model to mistake a time period when the source is off with a modal interference null. To be consistent with the signal processing of the data, the modeled acoustic field underwent the same signal processing before computing the error function on each sampling of the geophysical space. This necessitated the selection of a simple seabed model, a single layer, but with the physics of overburden pressure and sound speed and attenuation frequency dispersion constrained by causality.

A source of uncertainty in this work is that the mud layer may have a thin surface layer, and this layer was not considered in this study. It was found that the five data samples in the 1.5–4.0-kHz band did not appear to support inferring for the geophysical parameters for a two-layer mud model. Thus, the one-layer model should be viewed as an *effective* model for the mud sediment.

The VGS model with the depth dependence modification predicts a large nonlinear sound speed gradient in the mud sediment in the 1.5–4.0-kHz band. Over the larger 25–4000-Hz band while the size of the gradient decreases with decreasing frequency, the frequency dispersion of the sound speed increases with increasing depth into the sediment. Finally, future work is needed to understand the dispersion at the very low frequencies.

Acknowledgment

The authors would like to thank the crew of *RV Endeavor*.

References

[1] P. S. Wilson, D. P. Knobles, and T. B. Neilsen, "Guest editorial: An overview of seabed characterization experiment," *IEEE J. Ocean. Eng.*, vol. 45, no. 1, pp. 1–13, Jan. 2020.

[2] R. T. Cox, "Probability, frequency, and reasonable expectation," *Amer. J. Phys.*, vol. 14, pp. 1–13, 1946.

[3] D. C. Twichell, C. E. McClennen, and B. Butman, "Morphology and process associated with the accumulation of the fine-grained sediment deposit on the Southern New England Shelf," *J. Sedimentary Petrology*, vol. 51, pp. 269–280, 1981.

[4] J. A. Goff, J. Chaytor, A. Reed, G. Gawarkiewicz, P. S. Wilson, and D. P. Knobles, "Stratigraphic analysis of a sediment pond within the New England Mud Patch: New constraints from high-resolution chirp acoustic reflection data," *Marine Geol.*, vol. 412, pp. 81–94, 2019.

[5] J. Chaytor, M. Ballard, Z. Buczkowski, J. A Goff, K. M. Lee, and A. Reed, "Measurements of geologic characteristics, geophysical properties, and geoacoustic response of sediments from the New England Mud Patch," *IEEE J. Ocean. Eng.*, accepted for publication.

[6] M. J. Buckingham, "Wave propagation, stress relaxation, and grain-to-grain shearing in saturated, unconsolidated marine sediments," *J. Acoust. Soc. Amer.*, vol. 108, pp. 2796–2815, 2000.

[7] M. J. Buckingham, "On pore-fluid viscosity and the wave properties of saturated granular materials including marine sediments," *J. Acoust. Soc. Amer.*, vol. 122, pp. 1486–1501, 2007.

[8] M. J. Buckingham, "Compressional and shear wave properties of marine sediments: Comparisons between theory and data," *J. Acoust. Soc. Amer.*, vol. 117, pp. 137–152, 2005.

[9] M. J. Buckingham, "Wave speed and attenuation profiles in a stratified marine sediment: Geo-acoustic modeling of seabed layering using the viscous grain shearing (VGS) theory," *J. Acoust. Soc. Amer.*, vol. 148, no. 2, pp. 962–974, 2020.

[10] A. Mallock, "The damping of sound by frothy liquids," *Proc. Roy. Soc.*, vol. 84A, no. 572, pp. 391–395, 1910.

[11] A. B. Wood, *A Textbook of Sound*, 1st ed. New York, NY, USA: MacMillan, 1930.

[12] D. P. Knobles *et al.*, "Maximum entropy derived statistics of sound speed structure in a fine-grained sediment inferred from sparse broadband acoustic measurements on the New England Continental Shelf," *IEEE J. Ocean. Eng.*, vol. 45, no. 1, pp. 161–173, Jan. 2020.

[13] M. D. Richardson and K. B. Briggs, "Empirical predictions of seafloor properties based on remotely measured sediment impedance," in *High Frequency Ocean Acoustics*, M. Porter, M. Siderius, and W. A. Kuperman, Eds. College Park, MD, USA: AIP, 2004.

[14] W. C. Krumbein, "Size frequency distributions of sediments," *J. Sedimentary Petrology*, vol. 4, no. 2, pp. 65–77, 1934.

[15] H. A. Kramers, "La diffusion de la lumire par les atomes," *Atti Congresso Internationale Fisici (Trans. Volta Centenary Congr.) Como*, vol. 2, pp. 545–557, 1927.

[16] R. de L. Kronig, "On the theory of the dispersion of X-rays," *J. Opt. Soc. Amer.*, vol. 12, no. 6, pp. 547–557, 1926.

[17] L.D.Landau and E.M. Lifshitz, *Electrodynamics of Continuous Media*. Moscow, Russia: Pergamon, 1981.

[18] J. Belcourt, C. W. Holland, S. E. Dosso, J. Dettmer, and J. A. Goff, "Depth-dependent geoacoustic inferences with dispersion in the New England MudPatch via reaction coefficient inversion," *IEEE J. Ocean. Eng.*, vol. 45, no. 1, pp. 69–91, Jan. 2020.

[19] J. Bonnel, S. E. Dosso, D. Eleftherakis, and N. R. Chapman, "Trans-dimensional inversion of modal dispersion data on the New England Mud Patch," *IEEE J. Ocean. Eng.*, vol. 45, no. 1, pp. 116–130, Jan. 2020.

[20] J. Yang and D. R. Jackson, "Measurement of sound speed in fine-grained sediments during the seabed characterization experiment," *IEEE J. Ocean. Eng.*, vol. 45, no. 1, pp. 39–50, Jan. 2020.

[21] E. K. Westwood, C. T. Tindle, and N. R. Chapman, "A normal mode model for acoustoelastic ocean environments," *J. Acoust. Soc. Amer.*, vol. 100, pp. 3631–3645, 1996.

[22] I. Goodfellow, Y. Bengio, and A. Courville, *Deep Learning*. Cambridge, MA, USA: MIT Press, 2016, ch. 4.

[23] D. P. Knobles, J. D. Sagers, and R. A. Koch, "Maximum entropy approach for statistical inference in an ocean acoustic waveguide," *J. Acoust. Soc. Amer.*, vol. 131, pp. 1087–1101, 2012.

[24] D. P. Knobles, "Maximum entropy inference of seabed attenuation parameters using ship radiated broadband noise," *J. Acoust. Soc. Amer.*, vol. 138, pp. 3563–3575, 2015.

[25] S. Kullback and R. A. Leibler, "On information and sufficiency," *Ann. Math. Statist.*, vol. 22, pp. 79–86, 1951.

[26] E. T. Jaynes, "Information theory and statistical mechanics," *Phys. Rev.*, vol. 106, pp. 620–630, 1957.

[27] E. T. Jaynes, "Information theory and statistical mechanics: II," *Phys. Rev.*, vol. 108, pp. 171–190, 1957.

[28] G. Bilbro and D. E. Van den Bout, "Maximum entropy and learning theory," *Neural Comput.*, vol. 4, pp. 839–853, 1992.

[29] E. T. Jaynes *Probability Theory The Logic of Science.* Cambridge U.K.: Cambridge Univ. Press, 2007.

[30] M. S. Ballard, K. M. Lee, A. R. McNeese, P. S. Wilson, J. D. Chaytor, and J. A. Goff, "In situ measurements of compressional wave speed during gravity coring operations in the New England Mud Patch," *IEEE J. Ocean. Eng.*, vol. 45, no. 1, pp. 26–38, Jan. 2020.

David Paul Knobles received the Ph.D. degree in nuclear theory from the University of Texas at Austin, Austin, TX, USA, in 1989.

From 1989 to 1992, he did a Postdoctoral Fellowship in Nuclear Physics with the University of Texas at Austin. He is currently an owner of Knobles Scientific and Analysis (KSA), a private business that specializes in defense and environmental applications. His research interests include theoretical physics, remote sensing, cosmology, and bioacoustics.

Dr. Knobles is currently a Co-Chief Scientist for the ONR Seabed Characterization Experiment.

Christian D. Escobar-Amado received the Bachelor of Science degree in electronics engineering from the Francisco de Paula Santander University, Cucuta, Colombia, in 2016. He has been working toward the Ph.D. degree in electrical and computer engineering with the University of Delaware, Newark, DE, USA, since 2019.

From 2017 to 2018, he was a Junior Researcher with the Administrative Department of Science, Technology, and Innovation, also known as Colciencias, Bogotá, Colombia. His research interests include shallow water acoustics, Bayesian optimization methods, and physics-based deep learning techniques applied to ocean acoustics.

Dr. Escobar-Amado was awarded an internship with the Ocean Acoustic Engineering Laboratory, University of Delaware and subsequently admitted to the graduate program there.

Michael J. Buckingham received the B.Sc. (Hons.) degree in physics and the Ph.D. degree in solid state physics from the University of Reading, Reading, U.K., in 1967 and 1971, respectively.

He is currently a Distinguished Professor of Ocean Acoustics with the Marine Physical Laboratory, Scripps Institution of Oceanography (Scripps), University of California, San Diego, La Jolla, CA, USA. He has been a Visiting Professor with the Institute of Sound and Vibration Research, University of Southampton, Southampton, U.K., with the National Key Laboratory of Science and Technology on Sonar, Hangzhou, China, and with the Department of Ocean Engineering, Massachusetts Institute of Technology, Cambridge, MA, USA. Before joining Scripps, he was an Individual Merit Senior Principal Scientific Officer with the Royal Aerospace Establishment, Farnborough, U.K. While with RAE, he was an Exchange Scientist, attached to the British Embassy, with the Naval Research Laboratory, Washington, DC, USA. He authored a book *Noise in Electronic Devices and Systems* (Wiley, 1983), and he is a coeditor of *Sea Surface Sound 1994, Proceedings of the III International Meeting on Natural Physical Processes Related to Sea Surface Sound*. His research has been reported in more than 250 papers, articles, and reports in the scientific literature.

Dr. Buckingham was the U.K. National Representative on the Scientific Committee of the Marine Science and Technology (MAST) Programme, Commission of European Communities, Brussels, Belgium. Along with several other awards for his research on underwater acoustics, he was the recipient of the A. B. Wood Medal from the Institute of Acoustics, U.K., and the Pioneers of Underwater Acoustics Medal from the Acoustical Society of America. He is a Fellow of the Acoustical Society of America, the Institute of Acoustics (U.K.), and the Institution of Engineering and Technology (U.K.); and he is a Chartered Engineer (U.K.). Recently, he was honored to serve as the Vice President of the Acoustical Society of America. He is currently an Editor-in-Chief of the *Journal of Computational Acoustics*, and he was the Editor of Reviews in Physical Acoustics for the *Journal of Sound and Vibration*.

William S. Hodgkiss (Life Member, IEEE) received the Ph.D. degree in electrical engineering from Duke University, Durham, NC, USA, in 1975.

His current research interests are in the areas of signal processing, communications, propagation modeling, ambient noise, and environmental inversions, with applications of these to underwater acoustics and electromagnetic wave propagation.

Dr. Hodgkiss is a Fellow of the Acoustical Society of America.

Since 1978, he has been a Member of the Faculty of the Scripps Institution of Oceanography, University of California, San Diego, La Jolla, CA, USA, and a Member of Staff of the Marine Physical Laboratory.

Preston S. Wilson received the B.S. and M.S. degrees in mechanical engineering from The University of Texas at Austin (UT Austin), Austin, TX, USA, in 1990 and 1994, respectively, and the Ph.D. degree in mechanical engineering from Boston University, Boston, MA, USA, in 2001, all in mechanical engineering.

He is currently a Raymond F. Dawson Centennial Fellow in Engineering with the University of Texas at Austin, with joint appointments with the Mechanical Engineering Department and with ARL:UT. He was a Research Engineer with the Applied Research Laboratories (ARL:UT) from 1993 to 1997, Postdoctoral Fellow with Boston University from 2001 to 2003, and has been a faculty member with the UT Austin since 2003. He holds six U.S. patents, and is a Co-Founder of AdBm, Inc., Austin, TX, USA, operating in the underwater noise mitigation arena. His work has been reported in more than 360 peer-reviewed papers, conference proceedings, technical reports and published presentation abstracts. He is currently a Co-Chief Scientist for the ONR Seabed Characterization Experiment. His research areas are broadly focused on physical acoustics, underwater acoustics, engineering acoustics, and bioacoustics, with specific areas of interest in sound propagation in shallow water, in water-saturated sediments, bubbly liquid, and multiphase material.

Dr. Wilson was the recipient of the A.B. Wood Medal from the Institute of Acoustics U.K. He is a Fellow of the Acoustical Society of America (ASA), the Past-Chair of the Committee for Education in Acoustics of the ASA, a current member of the Executive Council of the ASA, and an Associate Editor for the *Journal of the Acoustical Society of America*.

Tracianne B. Neilsen (Member, IEEE) received the Ph.D. degree in physics from The University of Texas at Austin, Austin, TX, USA, in 2000.

She is currently an Associate Professor with the Department of Physics and Astronomy, Brigham Young University, Provo, UT, USA. Her Postdoctoral Research was completed with the Applied Research Laboratories, University of Texas at Austin, investigating iterative optimizations for source localization and seabed parameterization in shallow ocean environments. Since 2007, she has been a part-time Research Scientist; her focus shifted to optimizations for high-frequency seabed parametrization using the Biot model. For more than a decade, she was a part-time Assistant Professor with Brigham Young University and did research on jet noise source characterization. In May 2018, she became a full-time Professor and returned to underwater acoustics research. She has recently been applying deep learning in ocean acoustics.

Jie Yang received the B.S. degree in physics from the Ocean University of China, Qingdao, China, in 1999 and the Ph.D. degree in mechanical engineering from the Georgia Institute of Technology, Atlanta, GA, USA, in 2007.

Since 2007, she was a Postdoctoral Fellow supported by the U.S. Office of Naval Research and currently a Principal Physicist with the Applied Physics Laboratory, University of Washington, Seattle, WA, USA. Her research interests include both active and passive acoustics, with the former focusing on mid-frequency sound propagation and reverberation in littoral oceans and the latter on estimating wind speed and rain rate using ocean ambient sound and their relation to global water cycle and climate change.

Dr. Yang is a member of the Acoustical Society of America.

Mohsen Badiey received the Ph.D. degree in applied marine physics and ocean engineering from the Rosenstiel School of Marine and Atmospheric Science, University of Miami, Coral Gables, FL, USA, in 1988.

From 1988 to 1990, he was a Postdoctoral Fellow with the Port and Harbor Research Institute, Ministry of Transport in Japan. After his Postdoctoral Research, he became a faculty member with the University of Delaware, Newark, DE, USA, where he is currently a Professor of Electrical and Computer Engineering and joint Professor in Physical Ocean Science and Engineering. From 1992 to 1995, he was a Program Director and a Scientific Officer with the Office of Naval Research (ONR) where he was the team leader to formulate long-term naval research in the field of Acoustical Oceanography. His research interests are physics of sound and vibration, shallow water acoustics and oceanography, underwater acoustic communications, acoustic signal processing and machine learning, seabed acoustics, and geophysics.

Dr. Badiey is a Fellow of the Acoustical Society of America.

Transducer Model

Darrell R. Jackson

January 29, 2018

1 Introduction

The purpose of these notes is to develop an equivalent circuit for a spherically symmetric, piezoelectric acoustic transducer. The values of the various circuit elements are given in terms of physical parameters such as the electromechanical coupling coefficient, transducer mass, acoustic properties of water, etc. The utility of the model is in relating the transmitter voltage response and terminal impedance to parameters such as radiation resistance, and to allow prediction of the change in performance with burial in sediment. It appears to be possible to apply the equivalent circuit to non-spherical transducers if the directivity is not too great. The model to be developed will be used to obtain transmit voltage response on the maximum response axis (MRA) as well as the transducer impedance. As impedance depends on the total radiated power, the model cannot deal with highly directional transducers. For a linear array of length L, the ratio of power integrated over all solid angle to the same integral assuming omnidirectionsl behavior with pressure equal to that on the MRA is

$$D = \frac{2}{kL} \int_0^{kL/2} [\sin(kL\cos\theta/2)/(kL\cos\theta/2)]^2 du \ . \tag{1}$$

This factor approaches unity as kL approaches zero, that is, as the array becomes omnidirectional. The model deals with pressure, not power, so the square root of D is of interest. This is plotted as a function of frequency in Fig. 1 assuming an array length $L = 0.813$ m, as for the PS800 transducer. This figure suggests that, if the model is fitted to TVR, the error in impedance determination should be less than 10% for frequencies less than 1200 Hz, but that substantial error may occur at higher frequencies.

2 Equivalent Circuit

It will be assumed that the transducer is a spherical shell of outer radius a with area $A = 4\pi a^2$. All time-varying quantities such as pressure and voltage are assumed to have $\exp(i\omega t)$ time dependence. The acoustic pressure in the water is

$$p_w = s_L \frac{e^{-ikr}}{r} \ . \tag{2}$$

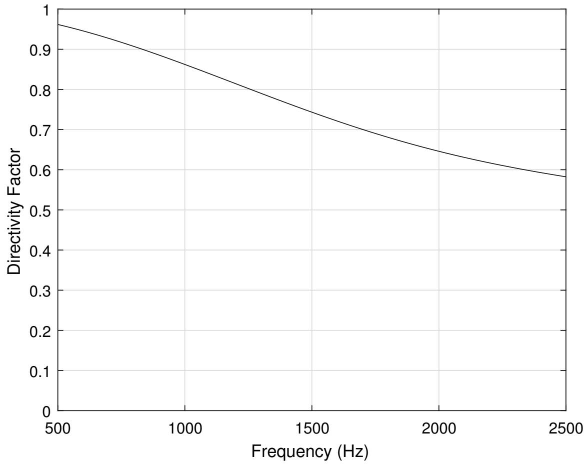

Figure 1: Square root of the power directivity factor D as a function of frequency.

The parameter s_L has dimensions pressure × length, and the source level is $20\log_{10}(|s_L|)$. The corresponding radial velocity of water molecules is

$$v_w = \frac{1+\frac{1}{ikr}}{\rho c} p_w \ . \tag{3}$$

Applying Newton's second law, the radial motion of the outer surface of the transducer is governed by the equation

$$i\omega m v = \alpha V - pA - Kx - \mu v \ , \tag{4}$$

where p and v are the pressure and radial velocity evaluated at $r = a$. The mass of the shell is denoted m, and α is a coefficient relating voltage V to the radial force produced by the piezoelectric effect. The parameter K is a spring constant giving the restoring force due to a displacement x, where $v = i\omega x$. Losses in the transducer are quantified by the parameter μ.

The main objective of this section is to determine the impedance $Z = V/I$ where V is the complex voltage introduced above, and the complex current is

$$I = i\omega C_0 V + \alpha v \ , \tag{5}$$

where C_0 is the capacitance of the transducer, and α is the electromechanical coefficient introduced earlier, here determining the current that results from polarization due to transducer motion. The various elements of the sought-after equivalent circuit are shown in Fig. 2.

Eliminating pressure as a variable through (3), velocity and voltage can be related as

$$\alpha V = (i\omega m + \frac{\rho c A}{1+\frac{1}{ika}} + \frac{K}{i\omega} + \mu) v \ . \tag{6}$$

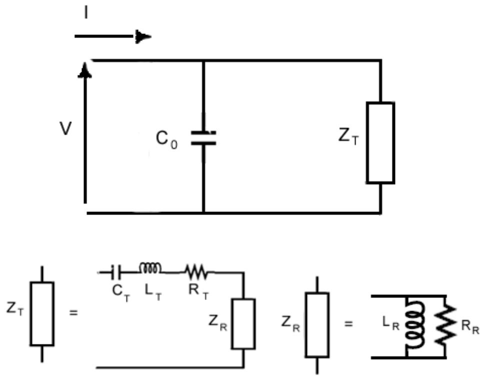

Figure 2: Upper: Definition of transducer voltage and current and decomposition of impedance into capacitance and circuit equivalents of electromechanical effects. Lower left: Decomposition of equivalent electromechanical components into those representing mechanical properties (subscript T) and those due to radiation (subscript R). Lower right: decomposition of radiation impedance into inductive (inertial) and radiative components.

Using this and (5), the transducer impedance is

$$Z = \frac{1}{1/Z_T + i\omega C_0} \ , \tag{7}$$

where

$$Z_T = i\omega L_T + \frac{1}{i\omega C_T} + R_T + Z_R \ . \tag{8}$$

Here,

$$L_T = \frac{m}{\alpha^2} \ , \tag{9}$$

is an inductance representing the inertia of the transducer,

$$C_T = \frac{\alpha^2}{K} \ , \tag{10}$$

is a capacitance representing elasticity of the transducer,

$$R_T = \frac{\mu}{\alpha^2} \ , \tag{11}$$

is a resistance representing power loss in the transducer, and

$$Z_R = \frac{1}{\frac{1}{R_R} + \frac{1}{i\omega L_R}} \tag{12}$$

is the radiation impedance consisting of a parallel combination of radiation resistance

$$R_R = \frac{\rho c A}{\alpha^2} \tag{13}$$

and an inductance representing inertia of the water

$$L_R = \frac{\rho a A}{\alpha^2} \ . \tag{14}$$

3 Transmit Voltage Response

The response of the transducer when used as a transmitter can be related to the equivalent circuit parameters. From (3) with $r = a$ and (6), the ratio of pressure at the transducer face to applied voltage is

$$\frac{p}{V} = \frac{\alpha Z_R}{4\pi a^2 Z_T} \ . \tag{15}$$

Using (13) to express α in terms of R_R, the pressure-voltage ratio at range r is

$$\frac{p_w(r)}{V} = \frac{1}{r}\sqrt{\frac{\rho c}{4\pi R_R}}\frac{Z_R}{Z_T}e^{-ik(r-a)} \ . \tag{16}$$

This is the complex transfer function for pressure in response to voltage. It can be used to determine the pulse distortion caused by frequency-dependent transmitter sensitivity. Note that the exponential propagation factor shows that propagation time is determined by the distance $r - a$, not by the range r to the center of the transducer. Taking the absolute value, the transmitter voltage sensitivity at range r is

$$S_0 = |\frac{p_w(r)}{V}| = \frac{1}{r}\sqrt{\frac{\rho c}{4\pi R_R}}|\frac{Z_R}{Z_T}| \ . \tag{17}$$

The units of pressure are determined by the units chosen for s_L. The TVR is $20\log_{10} S_0$.

4 Series Tuning

The previous discussion models the untuned transducer. In order to obtain an impedance match with the power amplifier and to increase TVR, an inductor may be added to cancel the largely capacitive reactance of the transducer. Figure 3 shows a tuning arrangement in which an inductor and resistor are added in series with the transducer. The resistor may be included to provide damping

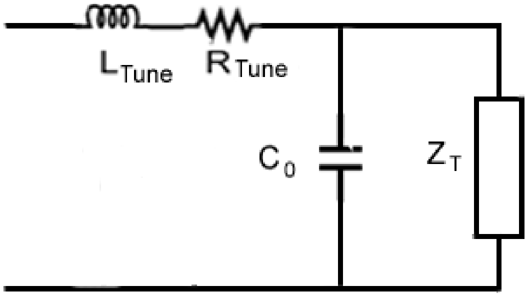

Figure 3: Circuit diagram for series tuning.

and an increase in bandwidth or it may simply be the unavoidable resistance of the actual inductor. The change in TVR can be modeled with little effort by noting that the voltage across the transducer terminals is the applied voltage V multiplied by the voltage-divider factor $Z/(Z+Z_{Tune})$, where

$$Z_{Tune} = R_{Tune} + i\omega L_{Tune} \ . \tag{18}$$

Thus (16) is modified to give the complex transfer function

$$\frac{p_w(r)}{V} = \frac{1}{r}\sqrt{\frac{\rho c}{4\pi R_R}}\frac{Z_R Z}{Z_T(Z+Z_{Tune})}e^{-ik(r-a)} \ , \tag{19}$$

and (17) becomes

$$S_0 = |\frac{p_w(r)}{V}| = \frac{1}{r}\sqrt{\frac{\rho c}{4\pi R_R}}|\frac{Z_R Z}{Z_T(Z+Z_{Tune})}| \ . \tag{20}$$

5 Receiving Sensitivity

The receiving voltage sensitivity can be obtained in similar fashion for the case of an incident plane wave. In the general case the wavelength may not be large compared to the transducer radius, so the average of incident pressure over the transducer face will be used. For a plane wave moving in the z-direction, the incident pressure is

$$p_i = p_{i0}e^{-ikz} \ . \tag{21}$$

The average over a sphere of radius a centered at the origin is

$$< p_i >= p_{i0}\frac{\sin ka}{ka} \ . \tag{22}$$

Receive sensitivity will be determined as the ratio of output voltage to $< p_i >$. The true sensitivity will be smaller by the factor given in (22).

The transducer will radiate in response to excitation by the plane wave, so the pressure at $r = a$ will be $p + < p_i >$, and the radial velocity will be $v + < v_i >$. Equation (3) with $r = a$ relates p and v, while $< p_i >= \rho c < v_i >$. Newton's second law is

$$i\omega m(v + < v_i >) = \alpha V - (p + < p_i >)A - K\frac{v + < v_i >}{i\omega} - \mu(v + < v_i >) \ . \quad (23)$$

The net current I into the transducer is assumed to be zero, so (5) gives

$$i\omega C_0 V + \alpha(v + < v_i >) = 0 \ . \quad (24)$$

Note the relation

$$p + < p_i > \ = \frac{\rho c(v + < v_i >)}{1 + \frac{1}{ika}} + \frac{< p_i >}{1 + ika} \ . \quad (25)$$

Using (23), (24),and (25), one obtains the ratio of transducer terminal voltage to incident pressure

$$M_T = |\frac{V}{< p_i >}| = \frac{1}{k}\sqrt{\frac{4\pi R_R}{\rho c}}|\frac{Z}{Z_T(1 + \frac{1}{ika})}| \ . \quad (26)$$

The receiving sensitivity is $20\log_{10} M_T$. This discussion does not include the effect of tuning, but extension to the tuned case is easy.

6 Reciprocity

The reciprocity relation for spherical transducers is

$$\frac{M_T}{S_T} = J_s \ , \quad (27)$$

where

$$J_s = \frac{2r}{f\rho} \ . \quad (28)$$

In the expressions above, f is the frequency, and S_T is the transmitting current sensitivity, related to the voltage sensitivity by the transducer input impedance defined earlier.

$$S_T = |Z|S_0 \quad (29)$$

Some algebra shows that (17) and (26) obey the reciprocity relation. This is the untuned case, but the tuned transducer must also obey reciprocity.

7 Fitting Model to Given TVR

The model parameters may be determined in two different ways. The first is to use knowledge of the transducer mechanical and piezoelectric properties to fix the values of the circuit elements. This information may not be available, and this approach becomes awkward for non-spherical transducers. A more practical method is to fit the model TVR to either the measured TVR or that supplied by the manufacturer. It is easiest to fit the untuned TVR, as it involves only five circuit elements, C_T, L_T, R_T, L_R, and R_R. Note that C_0 does not enter into the untuned TVR because it does not affect the terminal voltage.

One difficulty in this fitting process is that it is not unique: an infinity of choices for circuit element values will fit a given TVR, assuming it is consistent with the model. The approach to be used later in these notes is to find, by trial-and-error, one set of parameters that fits the untuned TVR, and then shift these values in such a way that the untuned TVR is not altered, but the tuned TVR can be fit with the fit constrained by the given values of L_{Tune} and R_{Tune}.

To show that the fitting process is not unique, (16) will be written in the form

$$\frac{p_w(r)}{V} = -\frac{1}{r}\sqrt{\frac{\rho c}{4\pi}}e^{-ik(r-a)} \tag{30}$$

$$\times \frac{\omega^2 L_R C_T R_R^{1/2}}{-i\omega^3 L_R L_T C_T - \omega^2 C_T(L_T R_R + L_R R_T + L_R R_R) + i\omega(L_R + R_T C_T R_R) + R_R} .$$

In this form it can be seem that all dependence on circuit parameters is contained in a rational function of frequency. If expanded in partial fractions, the transfer function would be decomposed into a sum of three poles whose positions in the complex ω-plane and residues are given in terms of circuit parameter values. There is no need to perform this decomposition, as the present purpose is to determine which parameter sets correspond to a given $p_w(r)/V$. Parameter values can be changed so long as they do not change this rational function. Dividing numerator and denominator by $L_R C_T R_R^{1/2}$, each of the coefficients in the denominator polynomial in ω must be unchanged. Taking the zeroth-order term in the polynomial first, one sees that

$$\frac{L_R C_T}{R_R^{1/2}} \tag{31}$$

must be unchanged as L_R, C_T, and R_R are changed. Using this, the first-order term requires that

$$\frac{L_R}{R_R} + R_T C_T \tag{32}$$

not change as L_R, C_T, R_R, and R_T are changed. The second-order and third-order terms require invariance of

$$L_T C_T + \frac{L_R R_T C_T}{R_R} + L_R C_T \tag{33}$$

and

$$\frac{L_R L_T C_T}{R_R} \ . \tag{34}$$

The main point is that there are four constraints on five circuit parameters. Thus, in five-dimensional parameter space, there is a one-dimensional curve, any point on which will give the specified TVR. If one takes R_R to be the independent variable, the other four parameters can be found in terms of R_R. This choice is arbitrary; any function of the five parameters could be taken as the independent variable. In the following, the dimensionless parameter

$$y = \frac{R_R}{R_{R0}} \tag{35}$$

will be taken as the independent variable, where R_{R0} is one member of an initial set of parameters R_{R0}, L_{R0}, R_{T0}, C_{T0}, and L_{T0} that have been found to fit the given TVR. The four constraints given above can be used to eliminate R_T, C_T, and L_T, giving the following cubic equation to be satisfied by L_R:

$$L_R^3 + aL_R^2 + bL_R + c = 0 \ , \tag{36}$$

where

$$a = -y(L_{R0} + R_{T0}R_{R0}C_{T0}) \ , \tag{37}$$

$$b = R_{R0}^2 C_{T0} L_{R0} y^2 (1 - \sqrt{y} + L_{T0}/L_{R0} + R_{T0}/R_{R0}) \ , \tag{38}$$

$$c = -R_{R0}^2 C_{T0} L_{T0} L_{R0} y^3 \ . \tag{39}$$

Following a standard method of solving cubic equations, define

$$p = -a^2/3 + b \ , \tag{40}$$

$$q = 2(a/3)^2 - ab/3 + c \ , \tag{41}$$

$$Q = (p/3)^3 + (q/2)^2 \ , \tag{42}$$

$$A = (-q/2 + \sqrt{Q})^{1/3} \ , \tag{43}$$

$$B = (-q/2 - \sqrt{Q})^{1/3} \ . \tag{44}$$

The solution for L_R is

$$L_R = A + B - a/3 \ . \tag{45}$$

The argument of the cube root for A is positive, and the positive real root is used. The argument for B is negative, and the negative real root $-(q/2+\sqrt{Q})^{1/3}$ is used.

Knowing L_R, the other parameters can be found from the constraint equations:

$$L_T = L_{T0}\sqrt{y} \ , \tag{46}$$

$$C_T = \frac{L_{T0}C_{T0}}{L_R}\sqrt{y} \ , \tag{47}$$

$$R_T = \frac{R_{R0}}{L_{R0}}\sqrt{y}[-L_{T0}L_{R0}y/L_R + L_{R0}(1 - \sqrt{y}) + L_{T0} + R_{T0}L_{R0}/R_{R0}] \ , \tag{48}$$

$$R_R = yR_{R0} \ . \tag{49}$$

8 Examples

The model will be applied to the PS800 transducer, even though it is not spherical as assumed in the model derivation. If one ignores the connection between values of the equivalent circuit components and physical parameters such as radius, electromechanical coefficient, etc., and if the directivity is not too great, this may be acceptable. The following equivalent circuit parameters were determined by trial and error to fit the manufacturer's untuned TVR: $C_{T0} = 10^{-7}$ f, $L_{T0} = 0.4$ H, $R_{T0} = 398\ \Omega$, $R_{R0} = 265\ \Omega$, $L_{R0} = 0.018$ H. While these values gave a good fit to the untuned TVR, they did not give a fit to the tuned TVR. In fitting the tuned TVR, the parameters $L_{Tune} = 0.097$ H and $R_{Tune} = 5\ \Omega$ are given by the manufacturer and cannot varied in the fitting process. The only adjustable parameter besides those determining the untuned TVR is the transducer capacitance, C_0, and no value could be found that gave a fit. To get around this impasse, the freedom to vary the parameters for the untuned TVR, as discussed in the previous section, was exploited.

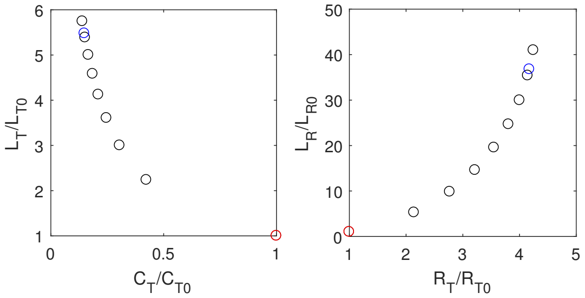

Figure 4: Illustration of the one-dimensional search through five-dimensional parameter space for parameters that allow a fit to the tuned TVR. The red circles mark the starting values C_{T0}, L_{T0}, R_{T0}, R_{R0}, L_{R0} given above. The starting value of the independent variable is $y = 1$ by definition. The black circles correspond to $y = 5,\ 9,\ 13,\ 17\ \cdots$, and the end point of the search is marked by a blue circle at $y = 30$.

The fitting was accomplish by trial-and-error adjustment of C_0 and y, with the value $y = 30$ allowing a reasonable fit to the tuned TVR (See Fig. 4). The final set of parameter values is $C_T = 1.49 \times 10^{-8}$ f, $L_T = 2.168$ H, $R_T = 1661\ \Omega$, $R_R = 7958\ \Omega$, $L_R = 0.6502$ H, $C_0 = 3.375 \times 10^{-7}$ f, $L_{Tune} = 0.097$ H, and $R_{Tune} = 5\ \Omega$. The fitted untuned and tuned TVRs are shown in Fig. 5. These TVRs are in good agreement with those supplied by the manufacturer.

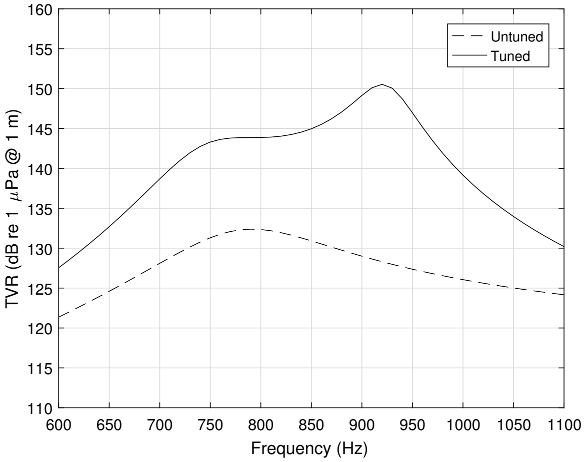

Figure 5: Fitted TVR for untuned and tuned cases for PS800 example.

It should be noted that the manufacturer's TVRs were obtained using a model and not directly measured. The manufacturer also provides the magnitude of the transducer input impedance as given by their model. The final circuit values given above yield the impedance magnitude shown in Fig. 6. This is in fair agreement with the manufacturer's model, but the agreement is not as good as for the untuned and tuned TVRs. This may in part be due to the directivity of the PS800.

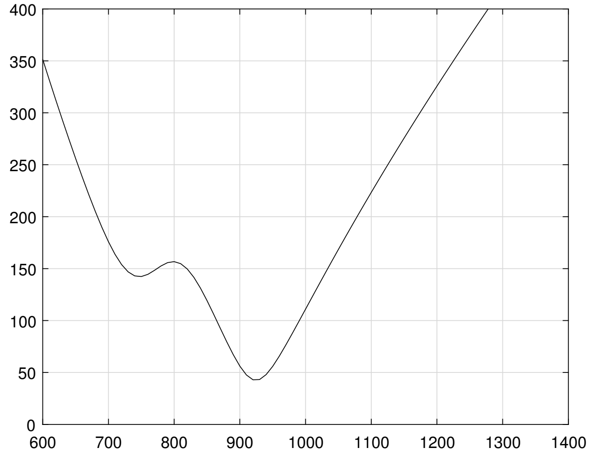

Figure 6: Absolute value of input impedance for tuned PS800 example.

9 Transducer Burial

Burial in sediment changes the density and sound-speed values in the model. If the sediment-water density and sound-speed ratios are a_ρ and ν_p, and if acoustic attenuation in the sediment is ignored, the model parameters are changed as follows:

$$R_{R\ Buried} = a_\rho a_p R_R \ , \tag{50}$$

$$L_{R\ Buried} = a_\rho L_R \ . \tag{51}$$

Here, R_R and L_R are for the in-water case. An additional change is required, as the square root of acoustic impedance appears as a factor in the transmitter pressure-voltage ratio (16). Thus, in addition to replacing the impedances Z_R, Z_T, and Z with altered values, an overall factor $\sqrt{a_\rho \nu_p}$ must be applied to the pressure-voltage ratio.

Figure 7 shows the tuned TVR before and after burial in a sediment with sound-speed ratio $\nu_p = 0.98$ and density ratio $a_\rho = 1.5$.

As seen in Fig 8, burial affects the transducer input impedance (this is Z, which does not include the tuning components). Although it has been assumed in the foregoing material that density is independent of frequency, poroelastic effects in sand can be accommodated by a fluid model with frequency-dependent effective density. Thus, poroelastic frequency-dependent density and sound speed can be readily incorporated in the transducer model. This suggests that measurements of receiver impedance might provide a means of measuring the depth profile of effective density.

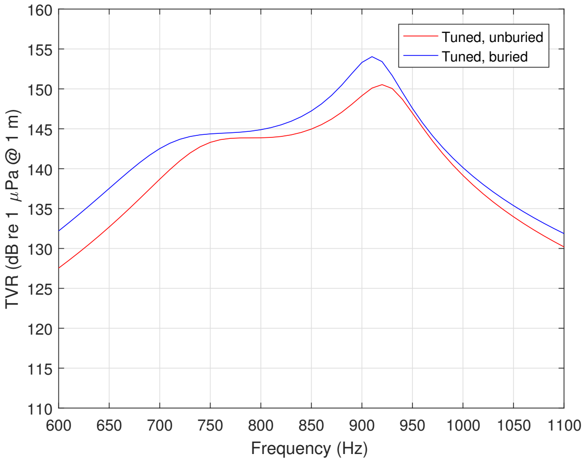

Figure 7: Tuned TVR for unburied and buried cases for PS800 example.

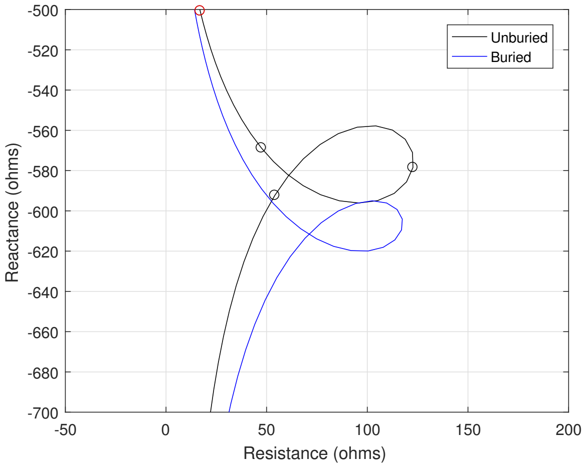

Figure 8: Impedance Z for PS800 example. The circles are spaced at 100-Hz intervals, with frequency decreasing going downward in the figure. The red circle marks 1000 Hz.

REPORT DOCUMENTATION PAGE

Form Approved
OMB No. 0704-0188

1. REPORT DATE *(DD-MM-YYYY)*
8/26/2021

2. REPORT TYPE
Final Technical

3. DATES COVERED *(From - To)*
4/1/2019 - 3/31/2021

4. TITLE AND SUBTITLE
Sediment Acoustics Modeling Using In Situ SAMS Data

5a. CONTRACT NUMBER

5b. GRANT NUMBER
N00014-19-1-2257

5c. PROGRAM ELEMENT NUMBER

6. AUTHOR(S)
Jie Yang

5d. PROJECT NUMBER

5e. TASK NUMBER

5f. WORK UNIT NUMBER

7. PERFORMING ORGANIZATION NAME(S) AND ADDRESS(ES)
University of Washington – Applied Physics Laboratory
4333 Brooklyn Avenue NE
Seattle, WA 98105-6613

8. PERFORMING ORGANIZATION REPORT NUMBER

9. SPONSORING / MONITORING AGENCY NAME(S) AND ADDRESS(ES)
Office of Naval Research / 322
875 North Randolph Street
Arlington, VA 22203-1995

10. SPONSOR/MONITOR'S ACRONYM(S)
ONR

11. SPONSOR/MONITOR'S REPORT NUMBER(S)

12. DISTRIBUTION / AVAILABILITY STATEMENT:

Distribution Statement A: Approved for public release; distribution is unlimited.

13. SUPPLEMENTARY NOTES

14. ABSTRACT

Naval sonar mission planning tools rely on simulation methods for propagation/reverberation modeling. One of the main limitations in making accurate predictions is the lack of a sufficiently detailed description of the environment. These environmental parameters include the properties of the sea bottom and water column over space and time. As inputs to real-time modeling, the water column properties, i.e., the sound speed profile and sea surface roughness, can be obtained in principle through direct measurements. However, sediment geoacoustic parameters, which are the most important parameters for predicting sound propagation and reverberation in many cases, are difficult to acquire directly, especially in the mid-frequency band. Work completed here and follow-on effort can be used to support detailed sound propagation prediction and validate geoacoustic inversion models, and hence, improve the accuracy in model predictions.

15. SUBJECT TERMS
In situ, SAMS, sediment sound speed and attenuation, sediment geoacoustic modeling, fine-grained sediments.

16. SECURITY CLASSIFICATION OF:			**17. LIMITATION OF ABSTRACT**	**18. NUMBER OF PAGES**	**19a. NAME OF RESPONSIBLE PERSON**
a. REPORT	**b. ABSTRACT**	**c. THIS PAGE**			Jie Yang
Unclassified	Unclassified	Unclassified	UU	55	**19b. TELEPHONE NUMBER** *(include area code)* (206) 543-1300

Standard Form 298 (Rev. 8-98)
Prescribed by ANSI Std. Z39.18